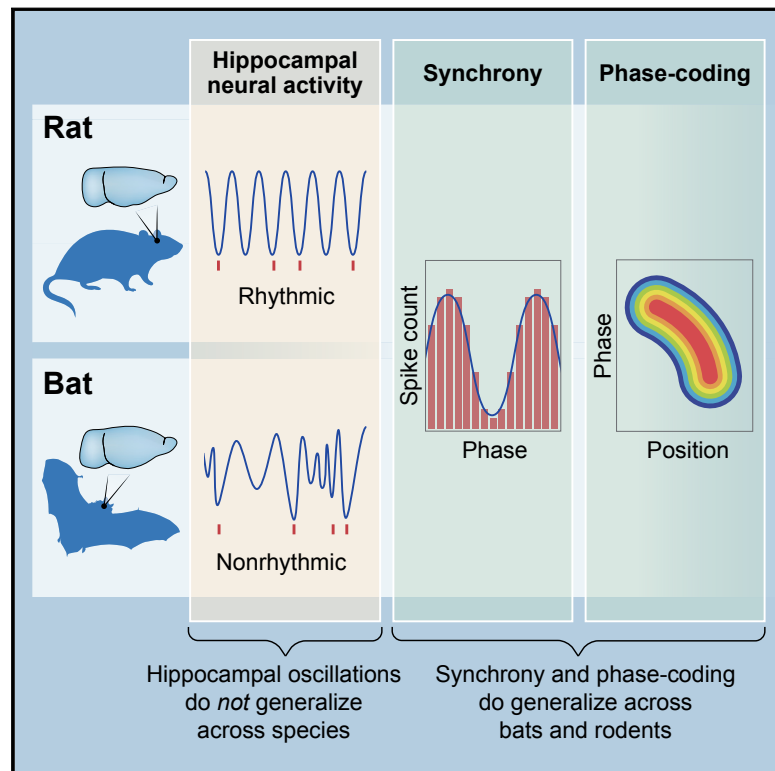# Nonoscillatory Phase Coding and Synchronization in the Bat Hippocampal Formation

Graphical Abstract

Authors

Tamir Eliav, Maya Geva-Sagiv, Michael M. Yartsev, Arseny Finkelstein, Alon Rubin, Liora Las, Nachum Ulanovsky

Correspondence

nachum.ulanovsky@weizmann.ac.il

In Brief

Measurements in freely moving bats reveal that hippocampal neurons encode the animal's position through temporal coding but in the absence of the oscillations observed in rodents.

Highlights

- Bat hippocampal neurons do not exhibit rodent-like theta oscillations

- Non-rhythmic synchronization and phase precession exist in bat place cells

- Demonstration of nonoscillatory phase coding in a mammalian brain circuit

- Synchrony and phase coding, but not oscillations, are conserved across bats and rodents

Article

Nonoscillatory Phase Coding and Synchronization in the Bat Hippocampal Formation

Tamir Eliav,[1] Maya Geva-Sagiv,[1,2,3,4] Michael M. Yartsev,[1,5] Arseny Finkelstein,[1,6] Alon Rubin,[1] Liora Las,[1] and Nachum Ulanovsky[1,7,*]

[1]Department of Neurobiology, Weizmann Institute of Science, Rehovot 76100, Israel
[2]ELSC Center for Brain Sciences, Hebrew University, Jerusalem 91904, Israel
[3]Present address: Department of Neurosurgery, University of California Los Angeles, Los Angeles, CA 90095, USA
[4]Present address: Sagol School of Neuroscience and Sackler School of Medicine, Tel Aviv University, Tel Aviv 69978, Israel
[5]Present address: Department of Bioengineering and the Helen Wills Neuroscience Institute, UC Berkeley, Berkeley, CA 94720, USA
[6]Present address: Janelia Research Campus, Howard Hughes Medical Institute, Ashburn, VA 20147, USA
[7]Lead Contact
*Correspondence: nachum.ulanovsky@weizmann.ac.il
https://doi.org/10.1016/j.cell.2018.09.017

SUMMARY

Hippocampal theta oscillations were proposed to be important for multiple functions, including memory and temporal coding of position. However, previous findings from bats have questioned these proposals by reporting absence of theta rhythmicity in bat hippocampal formation. Does this mean that temporal coding is unique to rodent hippocampus and does not generalize to other species? Here, we report that, surprisingly, bat hippocampal neurons do exhibit temporal coding similar to rodents, albeit without any continuous oscillations at the 1–20 Hz range. Bat neurons exhibited very strong locking to the non-rhythmic fluctuations of the field potential, such that neurons were synchronized together despite the absence of oscillations. Further, some neurons exhibited "phase precession" and phase coding of the bat's position—with spike phases shifting earlier as the animal moved through the place field. This demonstrates an unexpected type of neural coding in the mammalian brain—nonoscillatory phase coding—and highlights the importance of synchrony and temporal coding for hippocampal function across species.

INTRODUCTION

Brain oscillations have long been thought to play a major role in many brain functions (Buzsáki, 2006; Laurent, 2002; Singer, 2017). The rodent hippocampal formation—a brain region that was studied extensively in relation to spatial codes displayed by place cells (O'Keefe and Nadel, 1978; Wilson and McNaughton, 1993) and grid cells (Hafting et al., 2005; Barry et al., 2007)—is of particular interest for the study of oscillations, because in behaving rodents, the hippocampal formation exhibits a very prominent ∼8 Hz continuous rhythm called

the theta oscillation (Buzsáki, 2002). The theta oscillation was suggested to support functions as diverse as memory (Huerta and Lisman, 1993; Lisman and Jensen, 2013), navigation (O'Keefe and Recce, 1993; Skaggs et al., 1996), neural communication (Colgin et al., 2009), sequence learning (Skaggs et al., 1996; Mehta et al., 2002; Foster and Wilson, 2007), and lattice generation in grid cells (Burgess et al., 2007; Giocomo et al., 2007).

Recent findings from bats showed spatially tuned neurons in the hippocampal formation, including place cells (Ulanovsky and Moss, 2007; Yartsev et al., 2011; Yartsev and Ulanovsky, 2013), grid cells (Yartsev et al., 2011) and head direction cells (Finkelstein et al., 2015), with similar functional properties to rodents—but no continuous oscillations were found in bats at the theta frequency range (Ulanovsky and Moss, 2007; Yartsev et al., 2011; Yartsev and Ulanovsky, 2013). However, two major arguments were raised against the reported absence of theta oscillations in bats (Barry et al., 2012; Heys et al., 2013): (1) the frequency of oscillations could be lower in bats versus rats, as supported by *in vitro* experiments in bat entorhinal slices that revealed low-frequency membrane resonance (∼1.6–3.0 Hz) (Heys et al., 2013, 2016)—very different from the theta resonance reported in rodents (Giocomo et al., 2007; Heys et al., 2013), and (2) firing rates of bat neurons were claimed to have been too low to enable robust detection of oscillations (Barry et al., 2012; Climer et al., 2015). Therefore, before examining temporal coding in the bat hippocampus, we started off by addressing these two concerns and found no continuous oscillations at any frequency in the 1–20 Hz range—including not in hippocampal interneurons, which exhibit very high firing rates. However, bat neurons did exhibit very strong locking to the non-rhythmic fluctuations of the field potential at the 1–20 Hz range. These fluctuations synchronized neurons together; moreover, some neurons also displayed phase precession and phase coding of the bat's position relative to the "phase" of these non-rhythmic fluctuations. Our results suggest that normal hippocampal function entails synchronization of cell assemblies, as well as phase coding, which can be non-rhythmic as in bats or rhythmic as in rodents—but in both cases, the underlying neuronal coding principles might be surprisingly similar across species.

RESULTS

Bat Hippocampal Interneurons, Place Cells, and Grid Cells Do Not Exhibit Behavior-Related Oscillations, in Contrast to the Strong Theta Oscillations in Rats

We first focused on recording from hippocampal interneurons in Egyptian fruit bats, during both crawling and flight behaviors. Fast spiking interneurons are ideally suited for detecting oscillations—if these exist—because (1) interneurons exhibit very high firing rates (Figures 1A and 1B) and thus provide robust statistical power for identifying oscillations, (2) they are active nearly continuously, which facilitates detection of low-frequency rhythms (Climer et al., 2015), and (3) in rodents, hippocampal interneurons are highly theta-modulated—hence they are often called "theta cells" (Buzsáki, 2006). We recorded 44 putative interneurons from hippocampal area CA1 during crawling (n = 6 cells) or flight (n = 38 cells); interneurons were separated from pyramidal cells based on spike width and firing rate. To assess firing rate rhythmicity in single neurons, we computed the spike train autocorrelation for spikes emitted during behavior (see the STAR Methods). The autocorrelation was computed over a long timescale of ±2 s, to enable detection of possible slow oscillations at sub-theta frequencies. For comparison, we also computed the autocorrelations of published data from hippocampal and entorhinal neurons of rats (Hafting et al., 2005, 2008; Sargolini et al., 2006; Mizuseki et al., 2009). These rat neurons exhibited very strong theta oscillations (Figures 1C and 1D, bottom: note repetitive vertical bands). By contrast, the 44 bat interneurons exhibited rather flat autocorrelations (Figures 1A, examples, and 1D, top—population: no vertical bands). This suggests a lack of oscillatory modulation in bat interneurons, during either flight or crawling. Likewise, no oscillations could be readily observed in spatially tuned neurons: namely, bat hippocampal place cells recorded during crawling (n = 42) or in-flight (n = 55), as well as medial entorhinal cortex (MEC) grid cells recorded during crawling (n = 25) (Figure 1D, top: no vertical bands). Thus, qualitative visual inspection did not reveal oscillations in the spike trains of either interneurons, place cells, or grid cells.

Next, we systematically quantified possible rhythmicity in the spike trains of single cells by applying two different analysis methods (Royer et al., 2010; Deshmukh et al., 2010; Langston et al., 2010; Wills et al., 2010) (see the STAR Methods). First, we fitted the autocorrelations with a decaying cosine function (Figures 2A–2F and S1A–S1C), which allows detecting both high and low frequencies (Figures S1B and S1C). In rat neurons, this method successfully fitted large oscillatory components (Figure 2A, red lines denote the fit). By contrast, bat neurons did not exhibit substantial oscillations (Figure 2D). To quantify the oscillation strength, we defined a "temporal fit oscillation index" (see the STAR Methods). Rat neurons exhibited much higher values of the oscillation index as compared to bat neurons (Figures 2B versus 2E; two-sided t test, comparing the rat data in 2B to each of the bat datasets in 2E: $p < 10^{-20}$; $p < 10^{-14}$; $p < 10^{-3}$). While most rat neurons were significantly oscillatory (310/409, or 76%), very few bat neurons were significantly oscillatory (14/166, or 8.4%; see the STAR Methods). Moreover, the significant rat neurons were concentrated within a narrow fre-

quency band around the theta frequency (Figure 2C, dots cluster around ~8 Hz), while in the bat, those few cells that were significant were scattered across all possible frequencies (Figure 2F, dots do not cluster at any specific frequency). In a second analysis method, we computed the power spectrum of the autocorrelations (Figures S1D–S1I). Power spectra of rat neurons exhibited prominent peaks at the theta frequency (Figure 2G, see peak around ~8 Hz), usually accompanied by some power at very low frequencies, representing the slow decay in the autocorrelations (Figure 2G). By contrast, power spectra of bat neurons did not show any clear peaks at a single frequency in the 1–20 Hz range (Figure 2J). Similar to the temporal fit analysis, we computed a "spectral oscillation index" and best frequency for each neuron (see the STAR Methods). Rat neurons exhibited much higher oscillation index than bat neurons (Figure 2H versus 2K; two-sided t test, comparing the rat data in Figure 2H to each of the bat datasets in Figure 2K: $p < 10^{-5}$; $p < 10^{-5}$; $p < 10^{-6}$; $p < 10^{-3}$). Similar to the previous analysis, almost all rat neurons (332/409 or 81%) passed the oscillation significance test, while only a few of the bat neurons were found to be significantly oscillatory (9/166, or 5.4%), and the frequencies of these few significant bat neurons were much more scattered (Figure 2L; compare to Figure 2I for rats). Further, 67% of the rat neurons (273/409 cells) were detected to be significantly oscillatory by both the temporal fit and spectral analyses; and moreover, rat neurons exhibited the same frequency in both analyses (Figure 2M: blue dots fall primarily along the identity diagonal). By contrast, 0% of bat neurons (0/166 cells) were found by both methods to exhibit significant oscillations (Figure 2N). This finding strongly suggests that there are no behavior-related continuous oscillations at the 1–20 Hz range in bat hippocampal or entorhinal neurons.

Bat Neurons Exhibit Phase Locking to the Non-rhythmic LFP Fluctuations, which Synchronizes the Network

Notably, some models relating rodent theta oscillations to memory may not require strictly sinusoidal oscillations, but could function just as well with non-rhythmic fluctuations of the local field potential (LFP), as long as these fluctuations synchronize the network (Lisman and Jensen, 2013; Mehta, 2015; Kay et al., 2016). We thus hypothesized that it is the synchrony of cell assemblies, rather than their rhythmic periodicity, that is crucial for the proposed memory functions of the theta oscillation (Mehta, 2015). To explore this idea, we next examined the nature of LFP fluctuations in CA1 and MEC of behaving bats and whether these fluctuations synchronize the network's spiking activity.

Recordings in bat CA1 and MEC during behavior revealed large non-rhythmic fluctuations in the LFP (Figure 3A, top and middle traces), which had an approximately 1/f spectrum (Figure 3A, right panels; see similar plots also in Ulanovsky and Moss [2007] and Yartsev et al., 2011). Here, we analyzed the LFP only from crawling data and not flight data, because in flight the LFP signal (but not the single unit spikes) is often contaminated by wing beat artifacts. The LFP fluctuations were synchronized across different tetrodes (Figures S4E and S4F). Because spikes of rodent CA1 pyramidal neurons tend to phase lock slightly after the theta oscillation trough (Buzsáki, 2002) (as
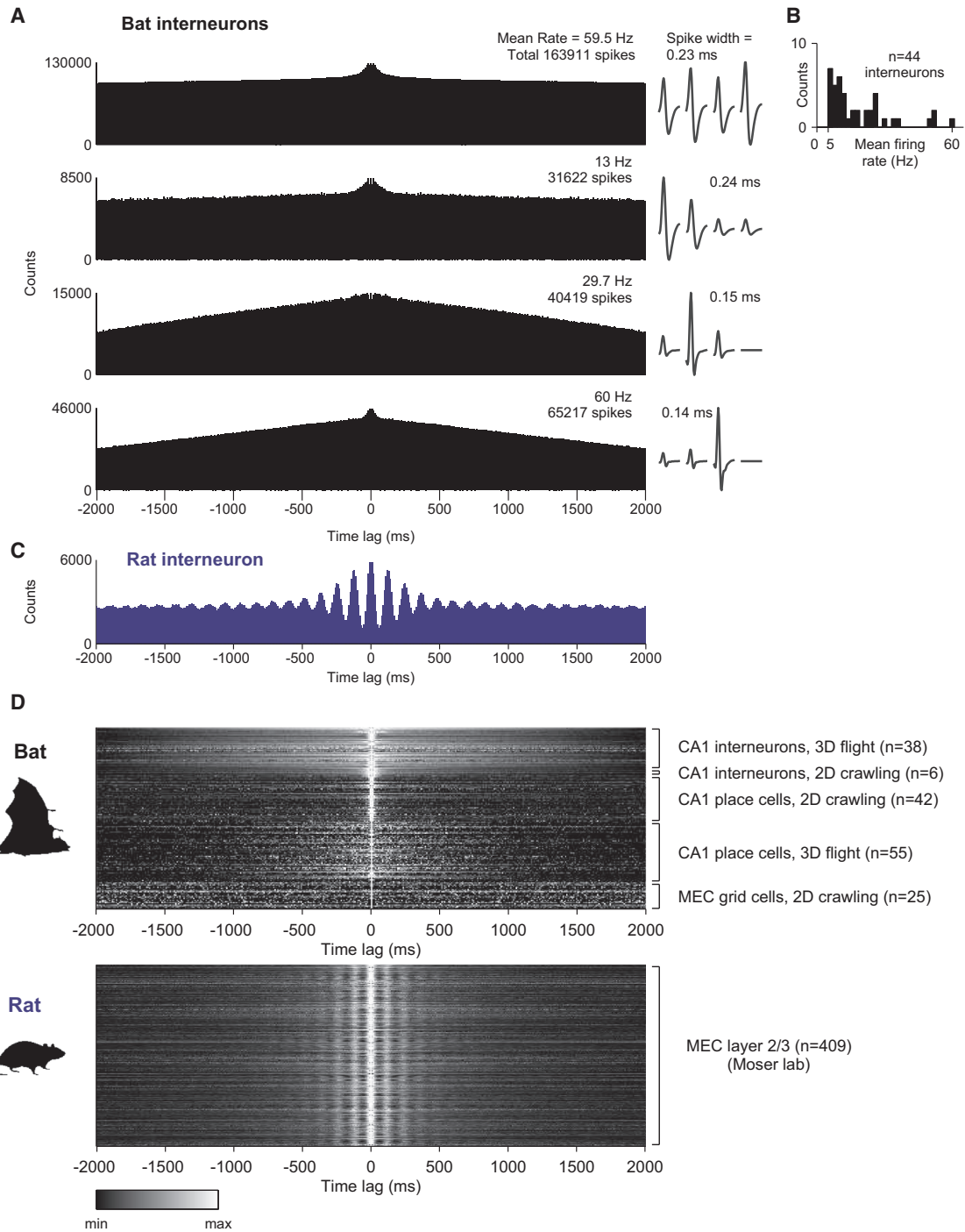
Figure 1. Spike Train Autocorrelations of Bat Interneurons, Place Cells, and Grid Cells

(A) Spike train autocorrelations of four example interneurons from bat CA1; range of time lags, ±2,000 ms; bin size, 10 ms. Shown are also their spike waveforms on the four channels of the tetrode, with spike widths indicated. The top two interneurons were recorded during crawling and the other two were recorded during flight.

(B) Histogram of mean firing rates of bat interneurons.

(C) Spike train autocorrelation of an interneuron from rat CA1, plotted for comparison. Same binning as for the bat.

(D) Top: autocorrelations of all 166 analyzed bat cells: interneurons (n = 38 in flight and n = 6 in crawling), 2D place cells (n = 42), 3D place cells (n = 55), and grid cells (n = 25). Rows, autocorrelations of single cells; grayscale normalized to min-max values of the autocorrelation for each neuron. Bottom: similar display for rat cells from medial entorhinal cortex (MEC) layer 2/3. Bin size, 10 ms. Same binning and graphical display for rats and bats. Rat data, courtesy of M.-B. Moser and E.I. Moser from: https://www.ntnu.edu/kavli/research/grid-cell-data. Note the vertical bands in the rat data at ~120-ms intervals, corresponding to the theta oscillation and the lack of any vertical bands in the bat data, indicating lack of continuous oscillations.
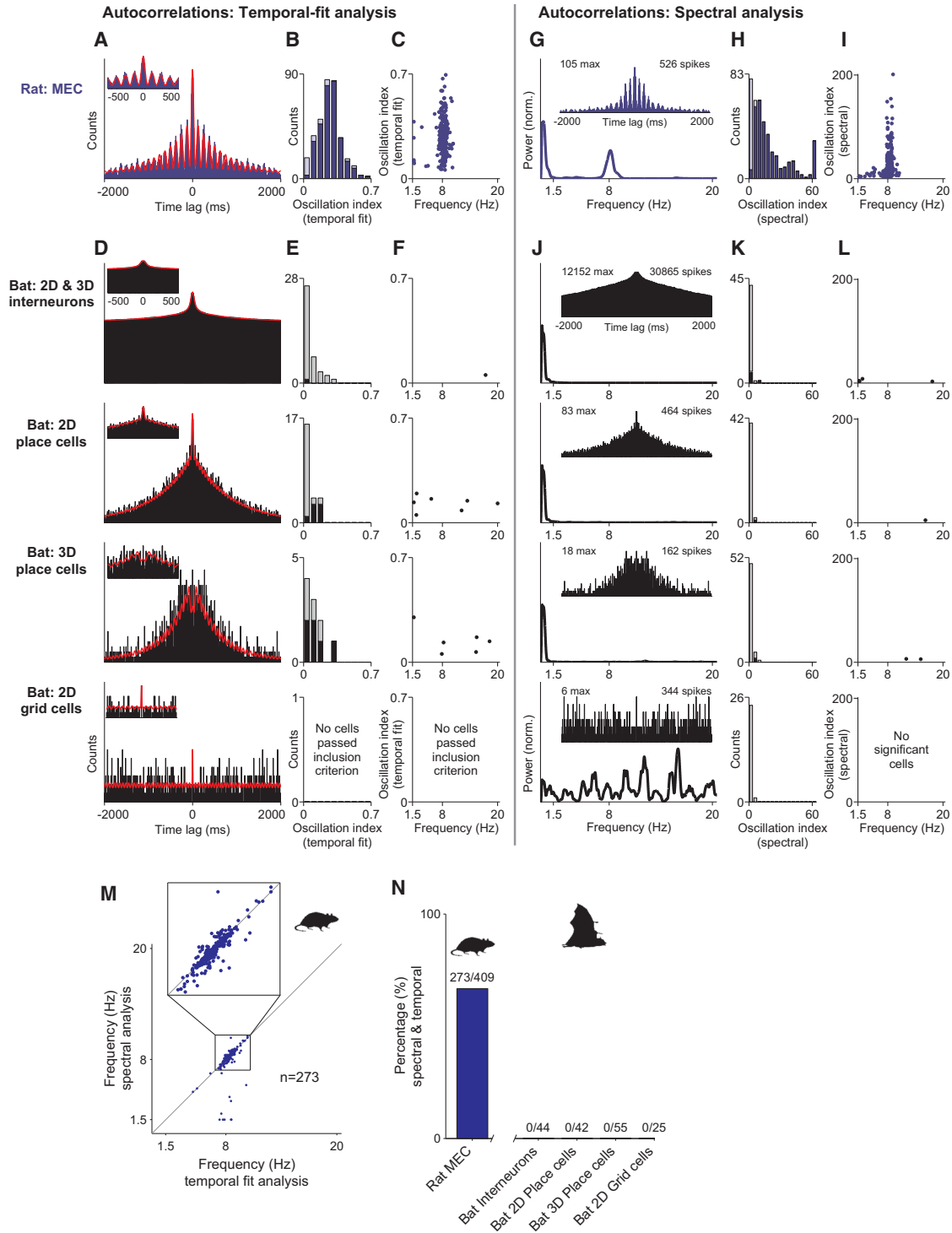
Autocorrelations: Temporal-fit analysis

Autocorrelations: Spectral analysis

A B C G H I

Rat: MEC

D E F J K L

Bat: 2D & 3D
interneurons

Bat: 2D
place cells

Bat: 3D
place cells

Bat: 2D
grid cells

M N

Figure 2. Absence of Behavior-Related Neuronal Oscillations in Bats

(A–F) Temporal fit analysis.

(A and D) Example neuron from each dataset (A, rat, in blue; D, bat, in black). Autocorrelations are overlaid with a fitted decaying sinewave function (red). Range of time lags, ± 2,000 ms; bin size, 10 ms. Inset: time lag zoom between ±500 ms. Same binning and graphical display for rat and bat.

(B and E) Distributions of oscillation index (temporal fit-based) for rats (B) and bats (E). Dark bars, significantly oscillatory cells; light-colored bars, non-significant cells. Datasets: rat MEC cells (n = 409), bat interneurons (n = 44, pooling together 38 cells recorded in flight and 6 cells in crawling), 2D place cells (n = 42), 3D place cells (n = 55), and grid cells (n = 25).

(legend continued on next page)

schematized in Figure 3B, bottom)—we hypothesized that in bats, pyramidal neurons would discharge slightly after the trough of the non-rhythmic LFP fluctuations (as schematized in Figure 3B, top: see red ticks). To test this, we computed the phase of each spike relative to the LFP fluctuations (Figure 3C). LFP phase was measured by filtering the LFP between 1–10 Hz, detecting the troughs (as in Figure 3C, inverted gray triangles), and then computing the cycle-by-cycle phase of the non-rhythmic LFP (0–360° for each cycle) by linearly interpolating the times between consecutive LFP troughs. To reduce noise in the phase estimation, we included only those LFP cycles (and spikes occurring within these cycles) that exceeded the 25% percentile of LFP power: this excluded the LFP cycles where the power was too low to allow reliable detection of the LFP troughs (see the STAR Methods). We found that, indeed, many neurons in bat CA1 and MEC exhibited phase locking to a particular phase of the LFP fluctuations (see examples in Figures 3D and 3F, top panels, and S5C). Spikes locked at a later time within long cycles than within short cycles, suggesting a phase locking mechanism rather than time locking mechanism (Figures S2A and S2B). Across all bat CA1 neurons, 47% of the place cells (14/30 neurons) and 38% of the nonspatial principal cells (5/13) exhibited significant phase locking (see the STAR Methods; binomial tests: $p < 10^{-10}$ and $p < 0.001$, respectively). Together, 44% of the CA1 principal cells (19/43) exhibited significant phase locking (binomial test, $p < 10^{-13}$). As a population, CA1 neurons showed phase locking around a phase of ∼30°, slightly after the trough of the local LFP fluctuations (Figure 3E, top)—very similar to theta phase locking in rat CA1 place cells (Buzsáki, 2002). Pooling spikes across cells yielded similar results (Figure 3E, bottom). In bat MEC, 20% of the grid cells (5/25 neurons) and 29% of the nonspatial principal cells (13/45) exhibited significant phase locking (binomial tests: $p < 0.01$ and $p < 10^{-6}$, respectively). Across the MEC population, phase locking tended to be around a phase of ∼200° (Figure 3G). Phase locking of spikes was also evident in spike-triggered LFP analysis (Figures 3H, left, and S3A, top plots—see distinct peaks at around t = 0 s). Note the lack of oscillations around this peak—in striking contrast to the prominent theta oscillations in rat spike-triggered LFP (Figures 3H, right, and S3B). Spike-triggered LFP analysis revealed phase locking of spikes across frequencies—both when the LFP traces

were filtered between 1–100 Hz prior to averaging (Figures 3H and S3A), as well as when the LFP was filtered between 1–10 Hz or between 10–20 Hz (Figure S3C). This indicates a rather broadband phase locking of spikes to LFP fluctuations, which was not limited to a particular frequency band. Notably, because bat LFP exhibited wide frequency changes over short periods of time (Figures 3A and S4A), the LFP frequency also occasionally passed through the theta band, yielding "theta bouts" (Figure S4B: see around t = 12 s)—that explains why in previous studies we found theta bouts, during which spikes exhibited theta locking (Ulanovsky and Moss, 2007; Yartsev et al., 2011). However, our new analyses suggest a notion that is rather different from that of oscillatory bouts—namely, the underlying process is that of non-rhythmic fluctuations to which the spikes are locked.

This notion was further supported by three additional analyses that we conducted (Figures 3D–3J). First, we examined spike phase versus instantaneous LFP frequency—this demonstrated a frequency-independent phase locking that occurred across all frequencies at a similar phase (Figures 3D and 3F, bottom panels; note the vertical stripes). Second, we examined the cycle-to-cycle variability of LFP frequencies during putative LFP bouts (see the STAR Methods)—and found that in the bat, the LFP frequencies were extremely variable, almost as variable as in a random shuffle (Figure 3J, compare black to gray)—and very different from the highly stable frequencies in the rat (Figure 3J, blue). A similar result was found when the same analysis was performed separately for specific frequency bands. In each of the analyzed frequency bands, from 1 to 20 Hz, bat LFP frequencies varied from cycle-to-cycle as much as expected from a random shuffle (Figures S4C, examples: compare the black lines [data] to the gray shaded areas [shuffle], and S4D, population; the separation into frequency bands was done by the frequency of the first cycle in each bout, while all subsequent cycles in the bout could be at any frequency). This demonstrates that hippocampal LFP in the bat is non-stationary, with variable cycle durations—which argues against an underlying oscillatory process. Third, we computed the spike-LFP coherence—a highly sensitive measure for detecting neural oscillations (Fries et al., 1997) (see the STAR Methods). We found that the coherence function in the bat was very flat and did not reveal any spectral

---

(C and F) Scatterplot of oscillation index versus fitted frequency, for all significant cells (dots). Note that in rats (C), nearly all the dots cluster around ∼8 Hz (theta), while in bats (F) there is paucity of significant dots, and moreover, the dots are scattered across all possible frequencies.

(G–L) Spectral analysis.

(G and J) Example neuron from each dataset. For each cell, the inset shows the spike train autocorrelation (with spike count and autocorrelation maximum indicated), and the main plot shows the power spectrum. Note the clear spectral peak at ∼8 Hz in the rat data (G) and the absence of such clear single peaks in the bat data (J).

(H and K) Distributions of oscillation index (spectral-based) for rats (H) and bats (K). Dark bars, significantly oscillatory cells; light-colored bars, non-significant cells; rightmost bar, oscillation index ≥60. Note the much larger values of the oscillation indices in rats versus bats.

(I and L) Scatterplot of the oscillation index versus extracted frequency, for all the significant cells (dots). Note that in rats (I), nearly all the dots cluster around 8 Hz (theta), while in bats (L) there are very few dots, and these dots are scattered across all possible frequencies.

(M) Combined temporal fit and spectral analyses for rat data. Scatterplot of fitted frequency in the spectral analysis (y axis) versus the temporal fit analysis (x axis). Inset: zoom around ∼8 Hz. Both analyses captured similar frequencies, as indicated by the clustering of dots around the diagonal identity line. Shown are only cells that passed the oscillation significance tests in both analysis methods (n = 273).

(N) Percentage of cells that were significantly oscillatory using both methods (conjunctively), plotted separately for each dataset. Note the large fraction of significantly oscillatory cells in the rat (273/409 cells, or 67%) versus the complete absence of significantly oscillatory cells in the bat (0/44 interneurons, 0/42 place cells in 2D, 0/55 place cells in 3D, and 0/25 MEC grid cells).
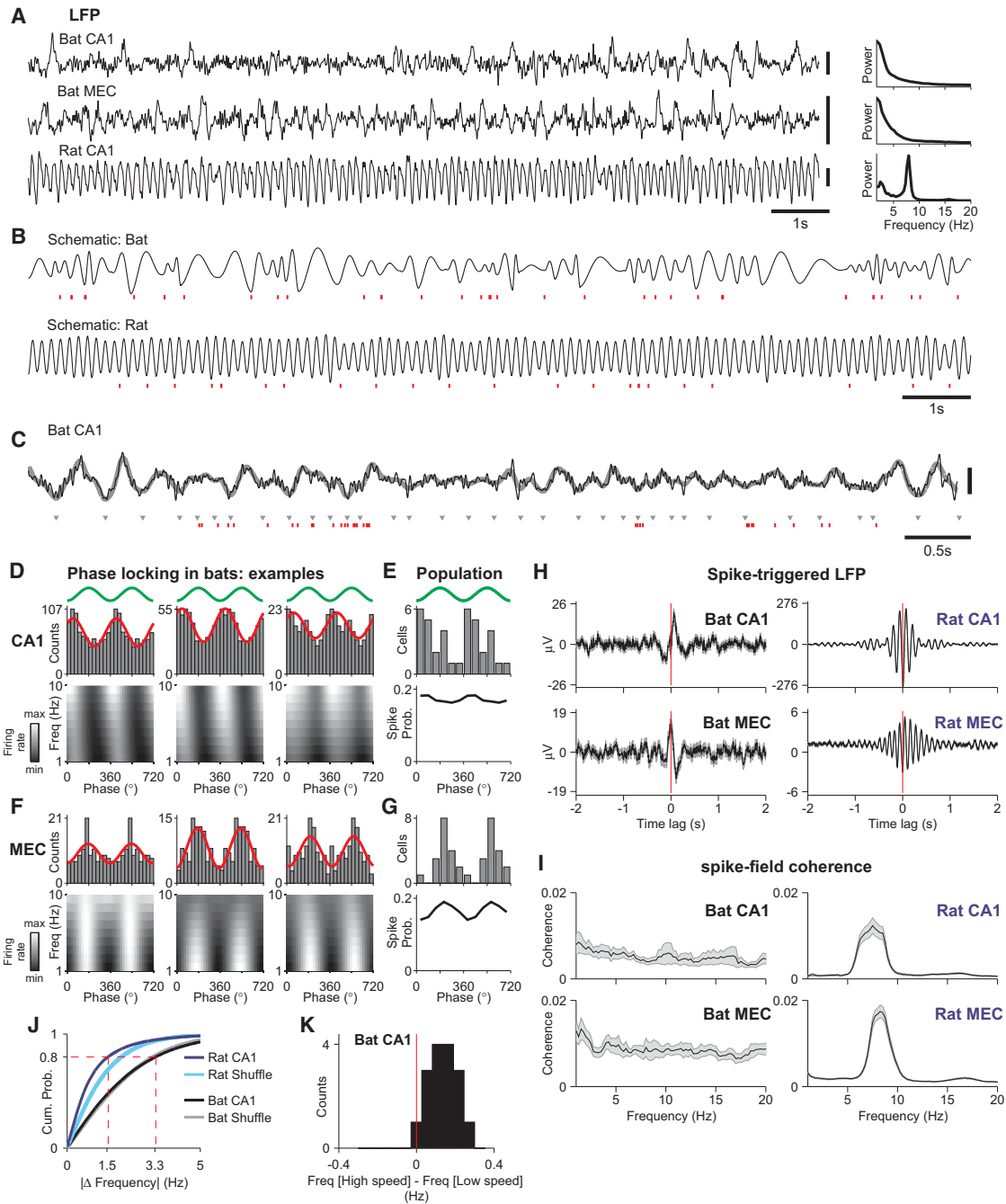
See also Figures S1 and S2.

Figure 3. Bat Neurons Exhibit Phase Locking to the Non-rhythmic LFP Fluctuations

(A) Left: LFP traces from bat CA1 (top), bat MEC (middle), and rat CA1 (bottom). Note the difference between the clearly rhythmic continuous oscillations in the rat versus the relatively irregular large fluctuations in the bat LFP, which did not exhibit continuous oscillations. The LFP traces were filtered between 1–40 Hz; positivity pointing up; scale bars, 1 s, 300 μV. Right: Power spectrum of the LFP for the entire recording session from which the trace on the left was taken. Bat data are from 2D arenas; CA1 and MEC traces were recorded from different bats. Rat CA1 data, courtesy of G. Buzsáki from http://crcns.org/data-sets/hc/hc-3.

(B) Schematic illustrating that spikes (red ticks) occur slightly after the LFP troughs in rat CA1 (bottom illustration) (Buzsáki, 2002); we hypothesized that in bats, similar phase locking of spikes might occur slightly after the trough of their non-rhythmic LFP fluctuations (top illustration). Scale bar, 1 s.

(C) Example of spike phase extraction; data from bat CA1. Black line, LFP (1–40 Hz). Gray line, LFP filtered 1–10 Hz; this filtering was used to identify LFP troughs (see gray inverted triangles). Red ticks, spikes. Scale bars, 0.5 s, 300 μV.

(D and F) Examples of 3 significantly phase-locked neurons recorded in bat CA1 (D) and 3 phase-locked neurons from bat MEC (F). Two cycles are shown for clarity. Top rows: spike phase histogram (bars); bin size, 30°; red line, cosine fit to the histogram. Bottom rows: frequency-by-phase firing rate maps. Green line,

(legend continued on next page)

peaks (Figure 3I, left)—in striking contrast to the large spectral peak seen in the rat coherence function at ∼8 Hz, in both CA1 and MEC (Figure 3I, right). Interestingly, we found that during crawling, the frequency of the non-rhythmic LFP fluctuations increased with the movement speed of the bat (Figure 3K; two-tailed t test comparing LFP frequency at high speeds [>median speed] versus low speeds [<median]: p < 10^{-5})—similar to the speed dependence of theta frequency in rats (Maurer et al., 2005; Buzsáki, 2006). This is an important result, because it indicates behavioral relevance for the nonoscillatory LFP fluctuations. Finally, spike-triggered LFP analysis for sleep data has demonstrated that CA1 neurons exhibited clear phase locking also during sleep (Figure S3D; we excluded from this analysis ±10-s epochs around each sharp-wave ripple in order to exclude any possible ripple-related locking); this suggests that phase locking occurs both during behavior and during sleep. Taken together, these results suggest that hippocampal-entorhinal circuits in bats use the non-oscillatory LFP fluctuations to synchronize neuronal cell assemblies, which could support the same functions that were proposed for theta oscillations in rodents—such as inter-regional communication, learning, and memory (Buzsáki, 2002, 2006; Mizuseki et al., 2009; Huerta and Lisman, 1993; Mehta, 2015).

Nonoscillatory Phase Precession and Phase Coding of Position in Bat Hippocampal Neurons

Next, we examined whether neurons in the hippocampal-entorhinal system of bats exhibit phase precession, similar to the phase precession in rodents (O'Keefe and Recce, 1993; Skaggs et al., 1996; Reifenstein et al., 2012), despite the non-rhythmic nature of the LFP in the bat. We employed a method used previously in rats (Mizuseki et al., 2009), which is particularly appropriate for analyzing phase precession in 2D environments and especially when the LFP is variable (see the STAR Methods). This method is based on computing the autocorrelation over the accumulated ("unwrapped") phases of the spikes relative to the LFP. For neurons that exhibit phase precession, this "phase autocorrelation" shows multiple peaks at a rate faster than the LFP (Mizuseki et al., 2009) (see examples from rat neurons in Figures 4A–4C and S5A, top). We found that, indeed, some neurons in the bat exhibited phase precession.

Figure 4D (middle) shows an example of phase precession in a bat CA1 place cell (note the autocorrelation peaks, marked by red arrowheads, occurred faster than integer multiples of the LFP cycle, marked by green dashed lines). Phase precession was less common than phase locking: 23% of the CA1 place cells (7/30 neurons) exhibited significant phase precession according to a shuffle analysis (see the STAR Methods; binomial test: p < 0.001; in MEC we also found examples of phase precession, as shown in Figure 4E, but the low amplitude of LFP recordings in MEC precluded systematic analysis). The power spectrum of these phase autocorrelations showed that the spiking activity was faster than the local LFP (Figure 4F: population average; see examples in Figure S5D), indicating phase precession.

Further, we directly examined whether there is also phase coding of spatial position—which is difficult to analyze in 2D, and therefore we linearized the animal's position to 1D (using trajectories that passed near the place field center; see the STAR Methods). Figure 4G shows an example cell whose spike phases were negatively correlated with the bat's spatial position (two leftmost panels: r = –0.47, p < 0.001). This systematic change of spike phases when passing through the place field was captured also by comparing the spike-triggered average LFP for spikes occurring in early positions versus late positions along the traverse (Figure 4G, right—note the phase shift between the green and red curves; additional examples in Figure S5E; STAR Methods). At the population level, there was a systematic difference between spike-triggered LFP traces computed using spikes occurring at early positions versus spikes occurring at late positions. This difference was manifested by negative correlations between LFP traces in early versus late positions (Figure 4H, magenta), as compared to positive correlations between similar locations (Figure 4H, cyan); this indicates that the timing of spikes relative to the LFP carried information about the animal's position. Such significant phase coding of position was found in 38% (16/42) of the CA1 place cells (binomial test: p < 10^{-10}). Thus, although phase precession and phase coding were less prevalent than phase locking, these results nevertheless suggest that neurons in the hippocampal formation of bats can exhibit nonoscillatory phase coding—a surprising form of neuronal temporal coding.

---

depiction of LFP phase (trough at 0°). Note that in both (D) and (F), the phase locking observed in the phase histograms (top rows) is maintained over a wide range of frequencies and is not limited to a specific frequency (bottom rows in D and F—notice the vertical stripes).

(E and G) Population analysis of phase locking for all the significantly phase-locked bat neurons (E, n = 19 cells from CA1; G, n = 18 cells from MEC). Green line, depiction of LFP phase (trough at 0°). Top: histograms of best-fitted phase for each cell (gray bars, counts of neurons); bin size, 60°. Bottom: spike phase firing probability: spikes were pooled across all significantly phase-locked neurons; bin size, 60°. Note that CA1 cells were locked slightly after the trough of the non-rhythmic LFP (phase ∼30°), similar to the theta locking at ∼30° in rat CA1 (Buzsáki, 2002), while MEC cells were locked to a different phase (∼200°).

(H) Left: spike-triggered LFP average, computed for all the spikes of bat CA1 neurons (top) and bat MEC neurons (bottom) that were included in (E) and (G). Right: spike-triggered LFP for rat data, plotted for comparison. The LFP traces, for both bat and rat data, were filtered between 1–100 Hz prior to averaging. Red line indicates time of spike; gray area, mean ± SEM.

(I) Spike-field coherence, computed for the data included in (H). Frequency bin, 0.25 Hz. LFP traces were filtered between 1–100 Hz prior to computing the coherence. Same filtering and binning were used for the bat and rat data. Gray area, mean ± SEM.

(J) Cumulative distribution of the changes in the frequencies of consecutive LFP cycles, computed only for cycles that occurred during putative bouts (see the STAR Methods). Dark blue line, rat data; black line, bat data; light blue area and gray area, 95% confidence intervals of the shuffled data for rat and bat, respectively. Red dashed lines indicate the frequency differences encompassing 80% of the data.

(K) LFP frequency in bat CA1 during crawling increased with movement speed—indicating the likely behavioral relevance of the nonoscillatory LFP fluctuations. Shown is a population histogram of frequency differences between LFP recorded during high movement speed of the bat (>median speed in the crawling session) versus low movement speed (<median); computed for sessions where place cells were recorded (n = 16 sessions).
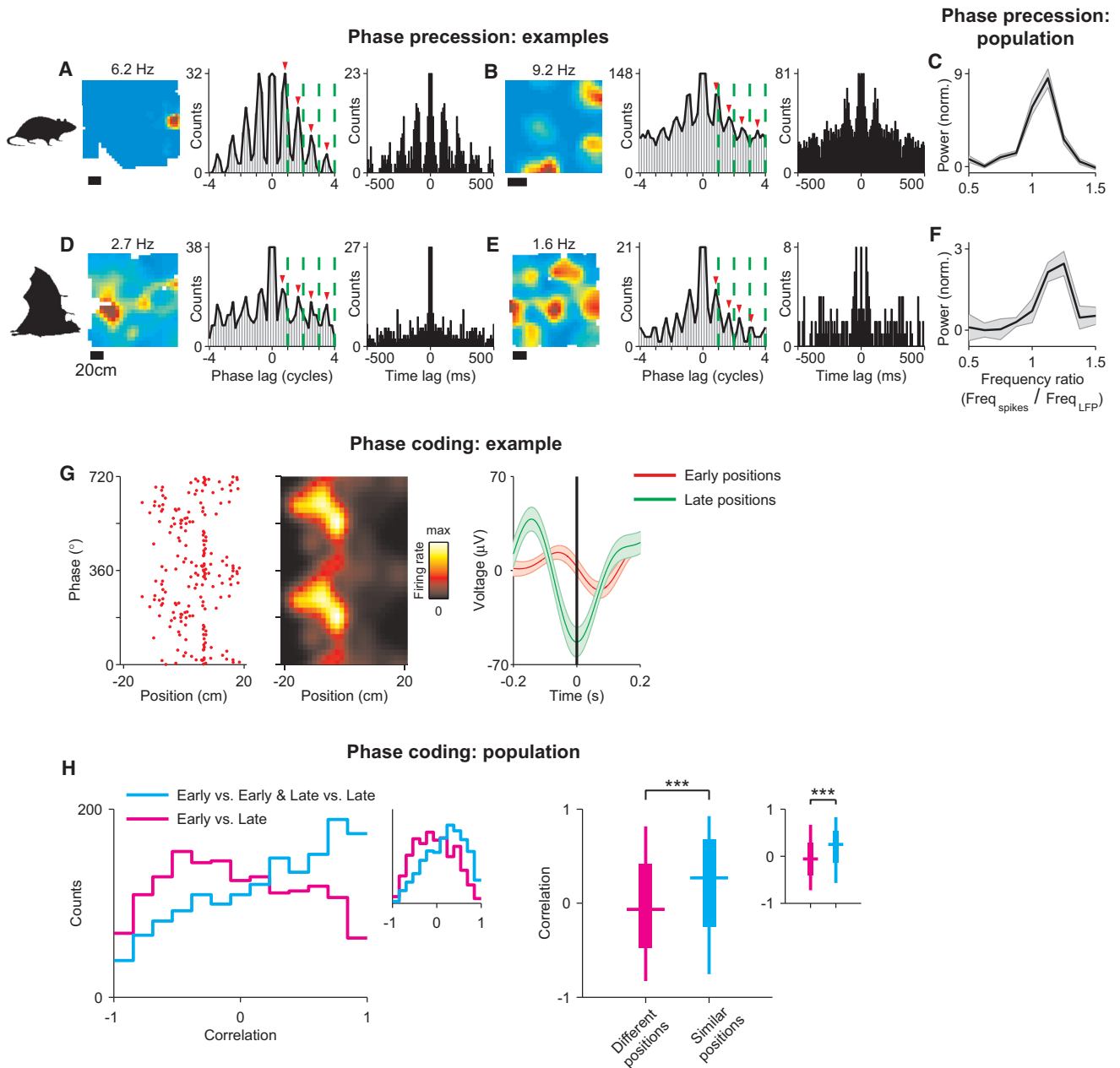
See also Figures S2, S3, S4, and S5.

Phase precession: examples

Phase precession: population

A 6.2 Hz

B 9.2 Hz

C

D 2.7 Hz

20cm

E 1.6 Hz

F

Phase lag (cycles) Time lag (ms) Phase lag (cycles) Time lag (ms)

Frequency ratio
(Freq$_{spikes}$ / Freq$_{LFP}$)

Phase coding: example

G

Early positions
Late positions

Phase coding: population

H

Early vs. Early & Late vs. Late
Early vs. Late

***   ***

Different positions   Similar positions

Figure 4. Nonoscillatory Phase Precession and Phase Coding in Bat Hippocampal Neurons

(A and B) Examples of a rat CA1 place cell (A) and a rat MEC grid cell (B), exhibiting phase precession. Left plots: Firing rate maps; scale bars, 20 cm. Middle plots: accumulated phase spike train autocorrelation (in short: "phase autocorrelation"; see the STAR Methods). Note that the peaks in these phase autocorrelations (red arrowheads) occurred faster than the LFP period (green dashed vertical lines), indicating phase precession. Right plots for each cell, standard spike train temporal autocorrelation (as in Figure 2). Note that the rhythmicity in these rat data is seen in both the phase autocorrelation (middle) and time autocorrelation (right). Rat MEC data, courtesy of M.-B. Moser and E.I. Moser from https://www.ntnu.edu/kavli/research/grid-cell-data; rat CA1 data, courtesy of G. Buzsáki from http://crcns.org/data-sets/hc/hc-3.

(C) Population analysis for rat data: Average power spectrum for all the significantly phase precessing rat neurons (n = 56 cells; see the STAR Methods). Gray area, mean ± SEM.

(D and E) Examples of a bat CA1 place cell (D) and a bat MEC grid cell (E), showing phase precession. Same conventions as in (A) and (B). Note the periodicity revealed in the phase autocorrelation (middle), which is not present in the time autocorrelation (right), indicating a non-rhythmic process.

(F) Population analysis for bat data: average power spectrum for all the significantly phase precessing bat CA1 neurons. Same conventions as in (C) (n = 7 cells; see the STAR Methods).

(G) Example of a bat CA1 place cell showing phase coding of the bat's position (linearized 1D position: see the STAR Methods). Left: negative correlation between spike phase and position. Middle: phase-by-position firing rate map. Right: spike-triggered LFP averages (filtered 1–6 Hz), calculated separately for spikes

(legend continued on next page)

Table 1. Prevalence of Phase Locking and Phase Coding in Bats versus Rodents

	Phase Locking	Phase Precession and Phase Coding
Bats (this study)	47% (place cells)	23% (place cells: phase precession)
	44% (principal cells)	38% (place cells: phase coding)
Rodents (published)	97% (rats: place cells); Schlesiger et al., 2015	74% (rats: place cells); Schlesiger et al., 2015
	84% (rats: principal cells); Mizuseki et al., 2009	88% (rats: principal cells); Mizuseki et al., 2009
	89% (rats: principal cells); Fujisawa and Buzsáki, 2011	55% (mice: place cells); Allen et al., 2011
		27% (mice: place cells); Zutshi et al., 2018

Comparison between CA1 place cells in bats versus rodents (rows) in terms of the percentage of significantly phase-locked neurons (left column) and significantly phase precessing and phase coding neurons (right column). Note that the different studies used different experimental setups (1D and 2D) and employed somewhat different metrics for quantifying phase coding and phase precession—hence the exact percentage values should be compared cautiously; nevertheless, it is clear that the percentages in bats are lower than in rodents.

DISCUSSION

Here, we reported several key results. First, we found that there was no spike train rhythmicity at any frequency in the 1–20 Hz range—in either bat interneurons, place cells, or grid cells, during either 2D or 3D locomotion (Figures 1 and 2). This strongly argues against classical "oscillatory interference models" of grid cells (Burgess et al., 2007; Giocomo et al., 2007), although some non-classical versions of the model may be compatible with our results (Orchard, 2015). Second, we found substantial phase locking of principal neurons in bat CA1 and MEC to the non-rhythmic LFP fluctuations (Figure 3)—consistent with a cross-species role for synchronicity in hippocampal function. It remains unclear why behavior-related fluctuations in the LFP of rodents are very rhythmic (i.e., theta oscillations), while LFP fluctuations in humans, monkeys, and bats tend to be non-rhythmic (Jacobs et al., 2007; Stewart and Fox, 1991; Ulanovsky and Moss, 2007; Yartsev et al., 2011) (although see Bohbot et al. [2017])—but our results suggest that in all these species, synchronicity of cell assemblies might play an important role. Third, we found that despite the absence of periodic rhythmicity in spike trains and in the LFP, some bat neurons exhibited rat-like phase precession and phase coding (Figure 4). To our knowledge, these results provide the first demonstration of nonoscillatory phase coding in any brain region of any species—a unique form of temporal coding.

The percentage of significantly phase-locked neurons in bat CA1 (47% of place cells, 44% of principal cells) was lower than the percentage of phase-locked neurons reported in rodent CA1 (~84%–97%; see Table 1). Likewise, the percentage of significantly phase coding neurons in bat CA1 (38% of place cells) was lower than reported in rodents (~27%–88%; see Table 1). This may indicate that the absence of oscillations re-

duces the propensity of hippocampal neurons to exhibit phase locking and phase coding. It remains to be seen in future experiments whether the percentage of phase-locked and phase coding neurons may increase during prolonged fast flight or in other subregions of the bat hippocampal formation. Nevertheless, we note that the percentages reported here in the bat are rather high and are very significant (binomial tests: $p < 10^{-10}$ for both phase locking and phase coding), demonstrating a decoupling between hippocampal theta oscillations, phase locking, and phase coding.

Why does the rodent hippocampus exhibit continuous theta oscillations, while the bat hippocampus does not? This remains an open question, and we can only speculate here. One possibility is that the medial septum—the brain region that is believed to serve as the primary pacemaker for hippocampal theta in rodents (Buzsáki, 2002)—lacks oscillatory neurons in bats. This should be tested in the future by recording from the bat medial septum. Another possibility is that the medial septum is oscillating in bats similarly to rodents, but it is unable to drive hippocampal or entorhinal oscillations because hippocampal formation neurons in the bat are not responsive at the theta frequency—as supported by the finding of lack of theta resonance in medial entorhinal neurons of bats (Heys et al., 2013). Importantly, however, our present study demonstrates a surprising inter-species similarity in terms of phase locking and phase coding. Notably, hippocampal LFP in monkeys (Stewart and Fox, 1991) and humans (Jacobs et al., 2007; Aghajan et al., 2017) tends to exhibit very little periodicity in the 1–20 Hz range, with the exception of possible oscillatory "bouts" that in humans last on average 3 cycles (Aghajan et al., 2017). It would be interesting to test whether hippocampal neurons in monkeys and humans exhibit nonoscillatory phase coding—similar to our findings in bats.

occurring in early positions (red) versus late positions (green); plotted as mean ± SEM; note the phase shift between early and late positions (compare red and green curves).

(H) Population analysis of all the significantly phase coding neurons in bats, using 1–6 Hz filtering (main plots: n = 16/42, or 38% significant cells), or using 1–10 Hz filtering (insets: n = 14/42, or 33% significant cells; see the STAR Methods). Left: distribution of spike-triggered LFP correlations between early versus late positions (magenta) and early-versus-early and late-versus-late positions (cyan). Right: boxplot of these distributions (horizontal line; median correlation; box, 25th and 75th percentiles; whiskers, 5th and 95th percentiles). Note the higher correlations when comparing similar positions (cyan, early-versus-early or late-versus-late) than when comparing different positions (magenta, early-versus-late; Wilcoxon rank sum test between the two distributions: $p < 10^{-30}$ for both 1–6 Hz and 1–10 Hz filtering), indicating that the timing of the spikes relative to the (irregular) LFP carried significant spatial information. See also Figure S5.
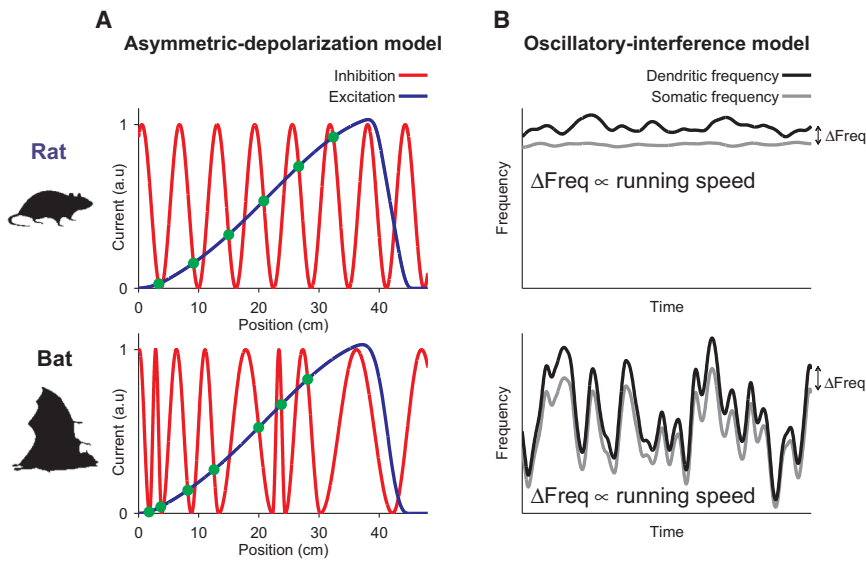
Figure 5. Models of Phase Precession

(A) Illustration of the asymmetric depolarization model (Mehta et al., 2002) using rhythmic oscillations (top: rat-like) versus non-rhythmic fluctuations (bottom: bat-like). The spikes in this model (green dots) occur when the down-swing of the fluctuating inhibitory current crosses the excitatory ramping current. Phase precession is obtained in both versions of this model, in both rats and bats: note that the spikes are advancing to earlier phases as the animal moves rightward through the place field.

(B) Illustration of the oscillatory interference model (O'Keefe and Recce, 1993; Burgess et al., 2007; Giocomo et al., 2007; Orchard, 2015) using rhythmic oscillations (top: rat-like) versus non-rhythmic fluctuations (bottom: bat-like). In both cases, the difference between the dendritic and somatic frequencies is proportional to the running speed of the animal, which allows integrating the animal's movements.

Our results are consistent with the asymmetric depolarization model of phase precession (Mehta et al., 2002), which does not require oscillatory activity and can operate with nonoscillatory fluctuations (Figure 5A, bottom). These data are also compatible with a non-classical oscillatory interference model that utilizes a non-rhythmic process (Orchard, 2015); however, the latter model requires some non-trivial assumptions—such as a mechanism to maintain two highly variable signals at a frequency difference precisely proportional to the movement speed (Figure 5B, bottom). Therefore, the asymmetric depolarization model seems a more likely possibility.

In summary, we found that bat hippocampal neurons did not exhibit behavior-related oscillations in the 1–20 Hz frequency band, but at the same time these neurons exhibited phase coding of position relative to the non-rhythmic fluctuations of the LFP. This finding provides a positive demonstration of nonoscillatory phase coding of a behavioral variable. We note that the nonoscillatory phase precession found here in bats may enable synaptic plasticity based on the firing order of neurons, thus supporting sequence learning—a key function proposed for phase precession in rodents (Skaggs et al., 1996; Mehta et al., 2002; Foster and Wilson, 2007). Taken together, these data suggest that, strikingly, a similar kind of temporal coding (phase coding) may be common to hippocampal function in both bats and rodents—and possibly also in primates. Further, our results dissociate between theta oscillations, cell assembly synchronicity, and phase coding of position—three phenomena that in rodents are tightly coupled together—whereas here we show that only the latter two phenomena generalize across species. This shift of focus from rhythmicity to synchronicity and temporal coding may reconcile some of the ongoing debates about the roles of oscillations in different species (Barry et al., 2012; Climer et al., 2015; Heys et al., 2013, 2016; Ulanovsky and Moss, 2007; Yartsev et al., 2011): Our results argue that, in terms of neural coding, there is, in fact, deep similarity across species.

STAR★METHODS

Detailed methods are provided in the online version of this paper and include the following:

- KEY RESOURCES TABLE
- CONTACT FOR REAGENT AND RESOURCE SHARING
- EXPERIMENTAL MODEL AND SUBJECT DETAILS
- METHOD DETAILS
  - Recording of hippocampal interneurons
  - Published datasets included in the analysis
  - Spike-train autocorrelations, and fitting a decaying-sinewave function
  - Oscillation index (temporal-fit) and its significance
  - Spectral analysis, and oscillation index (spectral) and its significance
  - LFP spectrum
  - LFP phase-locking
  - Phase-precession and phase-coding
- QUANTIFICATION AND STATISTICAL ANALYSIS
- DATA AND SOFTWARE AVAILABILITY

SUPPLEMENTAL INFORMATION

Supplemental Information includes five figures and can be found with this article online at https://doi.org/10.1016/j.cell.2018.09.017.

AUTHOR CONTRIBUTIONS

Conceptualization, T.E. and N.U.; Formal analysis, T.E.; Investigation, M.G.-S., M.M.Y., A.F., A.R., and L.L.; Writing, T.E. and N.U., with contributions from all authors; Supervision, N.U.

DECLARATION OF INTERESTS

REFERENCES

Allen, K., Fuchs, E.C., Jaschonek, H., Bannerman, D.M., and Monyer, H. (2011). Gap junctions between interneurons are required for normal spatial coding in the hippocampus and short-term spatial memory. J. Neurosci. 31, 6542–6552.

Barry, C., Hayman, R., Burgess, N., and Jeffery, K.J. (2007). Experience-dependent rescaling of entorhinal grids. Nat. Neurosci. 10, 682–684.

Barry, C., Bush, D., O'Keefe, J., and Burgess, N. (2012). Models of grid cells and theta oscillations. Nature 488, E1-2; discussion E2-3.

Boccara, C.N., Sargolini, F., Thoresen, V.H., Solstad, T., Witter, M.P., Moser, E.I., and Moser, M.-B. (2010). Grid cells in pre- and parasubiculum. Nat. Neurosci. 13, 987–994.

Bohbot, V.D., Copara, M.S., Gotman, J., and Ekstrom, A.D. (2017). Low-frequency theta oscillations in the human hippocampus during real-world and virtual navigation. Nat. Commun. 8, 14415.

Brandon, M.P., Bogaard, A.R., Schultheiss, N.W., and Hasselmo, M.E. (2013). Segregation of cortical head direction cell assemblies on alternating θ cycles. Nat. Neurosci. 16, 739–748.

Brun, V.H., Solstad, T., Kjelstrup, K.B., Fyhn, M., Witter, M.P., Moser, E.I., and Moser, M.-B. (2008). Progressive increase in grid scale from dorsal to ventral medial entorhinal cortex. Hippocampus 18, 1200–1212.

Burgess, N., Barry, C., and O'Keefe, J. (2007). An oscillatory interference model of grid cell firing. Hippocampus 17, 801–812.

Buzsáki, G. (2002). Theta oscillations in the hippocampus. Neuron 33, 325–340.

Buzsáki, G. (2006). Rhythms of the Brain (Oxford University Press).

Climer, J.R., DiTullio, R., Newman, E.L., Hasselmo, M.E., and Eden, U.T. (2015). Examination of rhythmicity of extracellularly recorded neurons in the entorhinal cortex. Hippocampus 25, 460–473.

Colgin, L.L., Denninger, T., Fyhn, M., Hafting, T., Bonnevie, T., Jensen, O., Moser, M.-B., and Moser, E.I. (2009). Frequency of gamma oscillations routes flow of information in the hippocampus. Nature 462, 353–357.

Csicsvari, J., Hirase, H., Czurkó, A., and Buzsáki, G. (1998). Reliability and state dependence of pyramidal cell-interneuron synapses in the hippocampus: an ensemble approach in the behaving rat. Neuron 21, 179–189.

Deshmukh, S.S., Yoganarasimha, D., Voicu, H., and Knierim, J.J. (2010). Theta modulation in the medial and the lateral entorhinal cortices. J. Neurophysiol. 104, 994–1006.

Finkelstein, A., Derdikman, D., Rubin, A., Foerster, J.N., Las, L., and Ulanovsky, N. (2015). Three-dimensional head-direction coding in the bat brain. Nature 517, 159–164.

Foster, D.J., and Wilson, M.A. (2007). Hippocampal theta sequences. Hippocampus 17, 1093–1099.

Fries, P., Roelfsema, P.R., Engel, A.K., König, P., and Singer, W. (1997). Synchronization of oscillatory responses in visual cortex correlates with perception in interocular rivalry. Proc. Natl. Acad. Sci. USA 94, 12699–12704.

Fujisawa, S., and Buzsáki, G. (2011). A 4 Hz oscillation adaptively synchronizes prefrontal, VTA, and hippocampal activities. Neuron 72, 153–165.

Geva-Sagiv, M., Romani, S., Las, L., and Ulanovsky, N. (2016). Hippocampal global remapping for different sensory modalities in flying bats. Nat. Neurosci. 19, 952–958.

Giocomo, L.M., Zilli, E.A., Fransén, E., and Hasselmo, M.E. (2007). Temporal frequency of subthreshold oscillations scales with entorhinal grid cell field spacing. Science 315, 1719–1722.

Hafting, T., Fyhn, M., Molden, S., Moser, M.-B., and Moser, E.I. (2005). Microstructure of a spatial map in the entorhinal cortex. Nature 436, 801–806.

Hafting, T., Fyhn, M., Bonnevie, T., Moser, M.-B., and Moser, E.I. (2008). Hippocampus-independent phase precession in entorhinal grid cells. Nature 453, 1248–1252.

Heys, J.G., MacLeod, K.M., Moss, C.F., and Hasselmo, M.E. (2013). Bat and rat neurons differ in theta-frequency resonance despite similar coding of space. Science 340, 363–367.

Heys, J.G., Shay, C.F., MacLeod, K.M., Witter, M.P., Moss, C.F., and Hasselmo, M.E. (2016). Physiological properties of neurons in bat entorhinal cortex exhibit an inverse gradient along the dorsal-ventral axis compared to entorhinal neurons in rat. J. Neurosci. 36, 4591–4599.

Huerta, P.T., and Lisman, J.E. (1993). Heightened synaptic plasticity of hippocampal CA1 neurons during a cholinergically induced rhythmic state. Nature 364, 723–725.

Jacobs, J., Kahana, M.J., Ekstrom, A.D., and Fried, I. (2007). Brain oscillations control timing of single-neuron activity in humans. J. Neurosci. 27, 3839–3844.

Kay, K., Sosa, M., Chung, J.E., Karlsson, M.P., Larkin, M.C., and Frank, L.M. (2016). A hippocampal network for spatial coding during immobility and sleep. Nature 531, 185–190.

Langston, R.F., Ainge, J.A., Couey, J.J., Canto, C.B., Bjerknes, T.L., Witter, M.P., Moser, E.I., and Moser, M.-B. (2010). Development of the spatial representation system in the rat. Science 328, 1576–1580.

Laurent, G. (2002). Olfactory network dynamics and the coding of multidimensional signals. Nat. Rev. Neurosci. 3, 884–895.

Lisman, J.E., and Jensen, O. (2013). The θ-γ neural code. Neuron 77, 1002–1016.

Aghajan, Z.M., Schuette, P., Fields, T.A., Tran, M.E., Siddiqui, S.M., Hasulak, N.R., Tcheng, T.K., Eliashiv, D., Mankin, E.A., Stern, J., et al. (2017). Theta oscillations in the human medial temporal lobe during real-world ambulatory movement. Curr. Biol. 27, 3743–3751.e3.

Maurer, A.P., Vanrhoads, S.R., Sutherland, G.R., Lipa, P., and McNaughton, B.L. (2005). Self-motion and the origin of differential spatial scaling along the septo-temporal axis of the hippocampus. Hippocampus 15, 841–852.

Mehta, M.R. (2015). From synaptic plasticity to spatial maps and sequence learning. Hippocampus 25, 756–762.

Mehta, M.R., Lee, A.K., and Wilson, M.A. (2002). Role of experience and oscillations in transforming a rate code into a temporal code. Nature 417, 741–746.

Mitra, P., and Bokil, H. (2007). Observed Brain Dynamics (Oxford University Press).

Mizuseki, K., Sirota, A., Pastalkova, E., and Buzsáki, G. (2009). Theta oscillations provide temporal windows for local circuit computation in the entorhinal-hippocampal loop. Neuron 64, 267–280.

Mizuseki, K., Sirota, A., Pastalkova, E., Diba, K., and Buzsáki, G. (2013). Multiple single unit recordings from different rat hippocampal and entorhinal

regions while the animals were performing multiple behavioral tasks. CRCNS. https://doi.org/10.6080/K09G5JRZ.

O'Keefe, J., and Nadel, L. (1978). The Hippocampus as a Cognitive Map (Oxford University Press).

O'Keefe, J., and Recce, M.L. (1993). Phase relationship between hippocampal place units and the EEG theta rhythm. Hippocampus *3*, 317–330.

Orchard, J. (2015). Oscillator-interference models of path integration do not require theta oscillations. Neural Comput. *27*, 548–560.

Reifenstein, E.T., Kempter, R., Schreiber, S., Stemmler, M.B., and Herz, A.V. (2012). Grid cells in rat entorhinal cortex encode physical space with independent firing fields and phase precession at the single-trial level. Proc. Natl. Acad. Sci. USA *109*, 6301–6306.

Royer, S., Sirota, A., Patel, J., and Buzsáki, G. (2010). Distinct representations and theta dynamics in dorsal and ventral hippocampus. J. Neurosci. *30*, 1777–1787.

Rubin, A., Yartsev, M.M., and Ulanovsky, N. (2014). Encoding of head direction by hippocampal place cells in bats. J. Neurosci. *34*, 1067–1080.

Sargolini, F., Fyhn, M., Hafting, T., McNaughton, B.L., Witter, M.P., Moser, M.-B., and Moser, E.I. (2006). Conjunctive representation of position, direction, and velocity in entorhinal cortex. Science *312*, 758–762.

Schlesiger, M.I., Cannova, C.C., Boublil, B.L., Hales, J.B., Mankin, E.A., Brandon, M.P., Leutgeb, J.K., Leibold, C., and Leutgeb, S. (2015). The medial entorhinal cortex is necessary for temporal organization of hippocampal neuronal activity. Nat. Neurosci. *18*, 1123–1132.

Singer, W. (2017). Neuronal oscillations: unavoidable and useful? Eur. J. Neurosci. Published online December 15, 2017. https://doi.org/10.1111/ejn.13796.

Skaggs, W.E., McNaughton, B.L., Wilson, M.A., and Barnes, C.A. (1996). Theta phase precession in hippocampal neuronal populations and the compression of temporal sequences. Hippocampus *6*, 149–172.

Stewart, M., and Fox, S.E. (1991). Hippocampal theta activity in monkeys. Brain Res. *538*, 59–63.

Ulanovsky, N., and Moss, C.F. (2007). Hippocampal cellular and network activity in freely moving echolocating bats. Nat. Neurosci. *10*, 224–233.

Wills, T.J., Cacucci, F., Burgess, N., and O'Keefe, J. (2010). Development of the hippocampal cognitive map in preweanling rats. Science *328*, 1573–1576.

Wilson, M.A., and McNaughton, B.L. (1993). Dynamics of the hippocampal ensemble code for space. Science *261*, 1055–1058.

Yartsev, M.M., and Ulanovsky, N. (2013). Representation of three-dimensional space in the hippocampus of flying bats. Science *340*, 367–372.

Yartsev, M.M., Witter, M.P., and Ulanovsky, N. (2011). Grid cells without theta oscillations in the entorhinal cortex of bats. Nature *479*, 103–107.

Zutshi, I., Brandon, M.P., Fu, M.L., Donegan, M.L., Leutgeb, J.K., and Leutgeb, S. (2018). Hippocampal neural circuits respond to optogenetic pacing of theta frequencies by generating accelerated oscillation frequencies. Curr. Biol. *28*, 1179–1188.e3.

STAR★METHODS

KEY RESOURCES TABLE

REAGENT or RESOURCE	SOURCE	IDENTIFIER
Deposited Data		
Rat MEC data	Moser lab	https://www.ntnu.edu/kavli/research/grid-cell-data
Rat CA1 data	Buzsáki lab	http://crcns.org/data-sets/hc/hc-3
Experimental Models: Organisms/Strains		
Egyptian fruit bats (*Rousettus aegyptiacus*)	Wild-born bats caught in Israel	N/A
Software and Algorithms		
MATLAB R2012b	MathWorks	https://www.mathworks.com/products/matlab.html
SpikeSort3D	Neuralynx	https://neuralynx.com/software/spikesort-3d
MATLAB Chronux Toolbox	Chronux	http://chronux.org/
Other		
Small animal stereotax	David Kopf Instruments	http://kopfinstruments.com/product/model-942-small-animal-stereotaxic-instrument-with-digital-display-console
Tetrode wire Platinum 90% Iridium 10% HML-insulated	California Fine Wire	http://www.calfinewire.com/index.html
Harlan 4 Drive	Neuralynx	https://neuralynx.com/hardware/harlan-4-drive
Digital Lynx 4SX	Neuralynx	https://www.neuralynx.com/hardware/digital-lynx-4sx
Small Animal Telemetry (SAT) system for electrophysiology	Neuralynx	SAT

CONTACT FOR REAGENT AND RESOURCE SHARING

Further information and requests for resources and reagents should be directed to and will be fulfilled by the Lead Contact, Nachum Ulanovsky (nachum.ulanovsky@weizmann.ac.il).

EXPERIMENTAL MODEL AND SUBJECT DETAILS

We collected data from adult male Egyptian fruit bats (*Rousettus aegyptiacus*), weighing 152 – 174 gr. Details of behavioral tasks and electrophysiological recordings are provided below. Neural recordings were conducted in the bat's dorsal hippocampus area CA1, and in the medial entorhinal cortex (MEC). We also analyzed publicly available data recorded by other laboratories from CA1 and MEC of rats: see details of these rat datasets below.

All experiments in Egyptian fruit bats were approved by the Institutional Animal Care and Use Committee of the Weizmann Institute of Science.

No randomization of animals was implemented, and experimenters were not blinded to animal group or behavioral task. Sample sizes for all experiments were determined based on previously published work, and statistical significance was determined post hoc.

METHOD DETAILS

Recording of hippocampal interneurons

Details of recordings methods are described in Geva-Sagiv et al. (2016). In brief: Adult male Egyptian fruit bats (n = 3) were trained either to fly back-and-forth in a linear flight setup (1.5-m length) or to crawl on an elevated platform (40 × 40 cm). After reaching good performance, animals were anesthetized with isoflurane (1 to 3%), placed in a stereotax (Kopf), and a four-tetrode microdrive (Neuralynx) was implanted above right dorsal hippocampal area CA1. The tetrodes (platinum-iridium 17.8-μm diameter wires, gold-plated to reduce the impedance to $\sim$500 kΩ) were then lowered toward the CA1 pyramidal cell layer. One tetrode was left in an electrically quiet zone and served as a reference. Recordings were conducted using either wired or wireless electrophysiology recording systems (Neuralynx DigitalLynx or Neuralynx SAT). Data were spike-sorted manually (Neuralynx SpikeSort3D). Although

in the past we found it difficult to record CA1 interneurons in-flight (Yartsev and Ulanovsky, 2013), in these 3 bats we succeeded to record a substantial number of interneurons. Recorded data consisted of a mixture of putative pyramidal cells and fast-spiking interneurons; we report here on the interneurons, which are the critical new cell type for analyzing neuronal rhythms in bats (n = 38 interneurons recorded in-flight, and n = 6 interneurons during crawling on the 2D platform). Putative interneurons were separated from putative pyramidal cells based on spike-width < 0.27 ms and mean firing-rate > 5 Hz; we did not apply a spatial-specificity criterion for separating the interneurons.

Published datasets included in the analysis

In addition to the new data from interneurons (some of which were recently published in Geva-Sagiv et al. [2016]), we also included in the analysis some previously published datasets that we recorded from Egyptian fruit bats: (1) Hippocampal CA1 place cells recorded during 2D-crawling in either a 117 × 117 cm square arena or a 62 × 62 cm square arena (n = 42 cells from 3 bats; data published in Yartsev et al. [2011] and Rubin et al. [2014]). (2) Hippocampal CA1 place cells recorded during 3D-flight in a large 5.8 × 4.6 × 2.7 m flight-room (n = 55 cells from 5 bats; data published in Yartsev and Ulanovsky [2013]). (3) MEC grid cells recorded during 2D-crawling in a 117 × 117 cm square arena (n = 25 cells from 3 bats; data published in Yartsev et al. [2011]).

Additionally, we analyzed data from MEC and CA1 of rats. The rat MEC data were taken from: https://www.ntnu.edu.kavli/research/grid-cell-data, courtesy of M.-B. Moser and E.I. Moser. The rat CA1 data were taken from: http://crcns.org/data-sets/hc/hc-3, courtesy of G. Buzsáki (Mizuseki et al., 2009, 2013).

Spike-train autocorrelations, and fitting a decaying-sinewave function

All analyses were done using MATLAB (Mathworks). For all types of neurons, in both bats and rats, we computed the spike-train autocorrelation over a ± 2,000-ms time window, using 10-ms bins; the long time-window of ± 2,000 ms was chosen to allow detecting slow oscillations, if they exist. The value of the autocorrelation at zero-lag was set to the maximal value across all other time-lags.

We fitted each spike-train autocorrelation with the following function:

$$f(t) = ae^{-\frac{|t|}{\tau_1}}(\cos(2\pi ft) + 1) + be^{-\frac{|t|}{\tau_2}} + ce^{-\frac{t^2}{\tau_3^2}} + d \tag{1}$$

Fitted parameter values were restricted to the following ranges (Royer et al., 2010): $a = [0, m]$, $b = [0, m]$, $c = [-m, m]$, $d = [0, m]$, $f = [1.5, 20]$ Hz, $\tau_1 = [0.1, 100]$ s, $\tau_2 = [0.1, 100]$ s, $\tau_3 = [0, 0.05]$ s; where m is the maximal value of the autocorrelation. To find the best fit, we performed the fitting 500 times with different random initial values for all the parameters; and for each of those 500 fits we computed the R^2 value between the original autocorrelation and the fit, and retained for further analysis the fit with the highest R^2 value. Only cells with $R^2 > 0.7$ (Brandon et al., 2013) and a maximal autocorrelation value > 10 were taken for population analysis (Figures 2B and 2E). This decaying-oscillation fit is an extension of a similar fit used previously to assess theta rhythmicity of spiking activity in rats (Royer et al., 2010). The main change in the form of the fit, as compared to the fit in Royer et al. (2010), was that we separated the decay time-constant into two time-constant parameters, one (τ_1) capturing the decay of the oscillatory component, and the other (τ_2) capturing the decay of the overall firing-rate component (see also examples in Figures S1B and S1C). The third decay time-constant (τ_3) captures the fast burst component, if it exists. In addition, we included a baseline firing-rate component (d), which allowed explicitly fitting a baseline: this was important due to the long time-window of ± 2,000 ms that we used for the autocorrelation. We allowed the fitted frequency, f, to go up to 20 Hz (double the maximal theta-frequency in rodents), and down to 1.5 Hz (the lower limit of expected frequencies based on *in vitro* membrane resonance measurements in Egyptian fruit bats [Heys et al., 2013]).

Oscillation index (temporal-fit) and its significance

We defined an index to capture the depth of oscillatory modulation in our decaying-oscillation fits, as follows:

$$oscillation\ index\,(temporal\ fit) = \frac{a}{\max(fit)}$$

where a is the amplitude of the oscillatory component, as fitted in Equation 1, and max(*fit*) is the maximal value of the fitted function in Equation 1.

To assess the significance of the oscillatory component a, we applied several criteria. First, we computed the 95% confidence interval for the fit of a, and required that it should be significantly positive – namely, that the 95% confidence-interval of the fitted value of a should be entirely above 0. Second, oscillation index (temporal-fit) had to be ≥ 0.05, signifying modulation depth of at least 5% of the total maximum firing-rate. Third, the decay of the oscillatory component to 5% of its maximal value should last for at least one period of the oscillation (1/f); thus we treated as non-oscillatory those cells that exhibited very fast decay of the oscillatory component ($3 \times \tau_1 < 1/f$), and retained cells which exhibited slower decay ($3 \times \tau_1 \geq 1/f$). If all three criteria were met, the cell was considered to be oscillatory at frequency f; these were the frequencies plotted on the x axis in Figures 2C and 2F.

Spectral analysis, and oscillation index (spectral) and its significance

We computed the spike-train autocorrelation for each cell, as described above, and then computed the power spectrum of the auto-correlation as the FFT-squared; the spectrum was normalized by its total power. We binned the spectrum using 1-Hz bins, running from 1.5 to 20.5 Hz, and computed the power in each spectral bin; this is the same frequency-range as in the temporal-fit analysis. To assess the significance at each bin, we repeated the same procedure for 2,000 shuffled spike-trains (see below for details on shuffling). We then found the frequency-bins that had significantly higher power in the real data than in the shuffled data ($p < 0.05$, Bonferroni-corrected for multiple bin comparisons, n = 19 bins). For all cells we used the distribution of shuffling spectra to compute the z-score of the spectral power at each frequency-bin, and chose the bin with the highest z-score to be the frequency-bin representing this cell ('peak-frequency'; see examples in Figures S1E, S1F, S1H, and S1I). Cells that had no significant frequency-bins, at any frequency, were regarded as non-oscillatory cells. The spectral-based oscillation index (x axis in Figures 2H and 2K) was taken as the ratio of the spectrum at the peak-frequency divided by the shuffle-mean at that frequency.

Generating shuffled spike trains: To create a null distribution for the spectral analysis (Figures 2G–2L), we modeled each cell's firing-rate based on its spatial firing properties (firing-rate map), as follows. Using the firing-rate map and the animal's movement trajectory, we computed the values of the expected firing-rate at each location (as derived from the firing-rate map), and then for each 10-ms time-bin on the trajectory we randomly generated spikes from a Poisson distribution, with the appropriate mean rate. For bursty-cell categories (place cells), or for interneurons which exhibited some burstiness (cells where the first moment of the auto-correlation [computed up to 50 ms] was < 25 ms; see Csicsvari et al. [1998]), we also modeled the bursty properties of the neuron by randomly choosing single spikes and turning them into bursts, to match the observed ratio of bursty/non-bursty spikes; the modeled bursts were drawn from the empirical distributions of the number-of-spikes per burst and of the inter-spike-interval, taken from the same neuron, while maintaining the mean empirical number of spikes for that neuron. Note that this method for generating shuffled spike-trains differs from using a fixed numerical threshold for the theta-index (Boccara et al., 2010), or from the random-shuffling method used previously in similar analyses (Barry et al., 2012; Yartsev et al., 2011; Yartsev and Ulanovsky, 2013). We used this method because uniform random shuffling creates a flat autocorrelation, and may therefore fail to capture the true shape of the experimental autocorrelations, which are often non-flat due to burstiness or due to behavior-induced temporal structure of the neural activity; our shuffling method, in contrast, gives more accurate estimates (see Figures S1D–S1I).

LFP spectrum

LFP spectra (Figure 3A, right) were computed using Welch's method (*pwelch* function in MATLAB) with Hamming windows (50% overlap). We used a window length of 4,096 samples, which equals 2.164 s.

LFP phase-locking

Analysis of phase-locking of spikes to the LFP (Figure 3) was conducted for all the bat neurons in which spikes were recorded simultaneously with high-quality LFP. This included all the 2D-crawling data from CA1 and MEC published in Yartsev et al. (2011) [CA1, n = 43 cells; MEC, n = 70 cells; both spatial and nonspatial cells; all the other datasets were excluded from this analysis because either they did not include LFP data at all, or the LFP quality was poor – specifically: (i) 3D place-cells and crawling-data from interneurons were recorded using telemetry equipment that high-passed all frequencies below 70 Hz, and thus did not permit low-frequency LFP recordings (Yartsev and Ulanovsky, 2013); (ii) flight-data from interneurons contained flight-related movement artifacts that corrupted the LFP signal]. For CA1 cells, the LFP was recorded from tetrodes located in the CA1 pyramidal cell layer; we only used LFP data from days when place-cells were recorded at the same time; the reference tetrode was located in an electrically quiet area in the corpus callosum above CA1. For MEC cells, the LFP was recorded from tetrodes located in all layers of MEC (Yartsev et al., 2011); we only used LFP data from days when grid-cells were recorded at the same time; the reference tetrode was located in an electrically quiet area. To measure the LFP phase, we filtered between 1–10 Hz the LFP traces that were recorded during behavior (with positivity pointing up); then the troughs were detected using a test for zero-derivative (as in Figure 3C, inverted gray triangles); and then we computed the cycle-by-cycle phase of the non-rhythmic LFP by linearly-interpolating between 0–360° the times of consecutive LFP troughs. To reduce noise in the phase estimation, we included only those LFP cycles (and spikes occurring within these cycles) that exceeded the 25% percentile of LFP power; this threshold excluded 25% of the LFP cycles where the power was too low to allow reliable detection of the LFP-troughs. We calculated the power of the LFP cycles as follows: We computed the power as the square of the absolute Hilbert transform of the filtered LFP signal, and then for each cycle of the LFP we assigned the mean power during the cycle. Applying this same LFP power-thresholding on the spike data did not affect our results on the non-rhythmicity of spike-trains (Figures S2C and S2D: here we extracted spikes only during LFP cycles that exceeded the 25% percentile of LFP power; note that in Figure S2D, the same number of neurons [dots] was above versus below the diagonal – indicating no systematic effect of the thresholding).

To test for *phase-locking*, we computed the histogram of spike phases, using a bin-size of 30°. Then, we fitted this histogram with the following cosine function: $a \cos(x - b) + c$ (see examples in Figures 3D and 3F, red lines). The preferred-phase of the neuron was taken as the fitted value of the parameter b (which is the phase where the cosine-fit reaches its maximum). Significance of phase-locking was defined as the significance of the Pearson correlation between the cosine-fit and the data.

To further examine the phase-relations between spikes and LFP across frequencies, we used the *spike-field coherence* measure (Fries et al., 1997), as follows (see Figure 3I; we used here the *mtspectrumc* function from the *Chronux* MATLAB toolbox,

http://chronux.org/ (Mitra and Bokil, 2007)). We extracted the LFP in a time-window of ± 2,000 ms around each spike, and calculated the spike-triggered average (STA) of the LFP in that window. The spike-field coherence was then computed as the ratio between the power spectrum of the STA, divided by the average of the power spectra of all the individual spike-triggered LFP traces (Fries et al., 1997).

To examine the *cycle-to-cycle variability in LFP frequency* (Figure 3J), we first identified putative 'bouts' in the LFP, as follows: Cycles with mean power higher than the median power were detected (with the median computed within the appropriate frequency bin), and then every two cycles which were separated in time by no more than their average duration were concatenated together to the same bout. We considered only bouts with overall duration ≥ 3 cycles. Next, we computed the cycle-to-cycle variability in the frequencies of consecutive cycles within those identified putative bouts (Figure 3J, black line and dark-blue line) – where the frequency of each cycle was taken as 1 divided by the cycle-duration. We then compared the cycle-to-cycle variability of the data to that of a shuffled version, by permuting the order of cycles 1,000 times, and taking the 95% confidence intervals of the shuffles (Figure 3J, gray area and light-blue area). We also repeated the analysis in Figure 3J separately for specific frequency bands, running from 1 to 20 Hz (Figures S4C and S4D). The separation into bands was done by the frequency of the first cycle in each pair of cycles: e.g., the 5–8 Hz band in Figure S4D means that the first cycle was in the 5–8 Hz range – but the subsequent cycle in the bout could be at *any* frequency.

Phase-precession and phase-coding

To examine whether there is *phase-precession* of spikes relative to the (irregular) LFP, we first applied a method introduced previously for rat data (Mizuseki et al., 2009): this method is particularly well suited for data collected in 2D open-field arenas, and for non-stationary LFP. We assigned to each spike its LFP cumulative phase (unwrapped phase), by accumulating the cycle-by-cycle phase from the beginning of the recording. Then we computed the autocorrelation of these cumulative-phases of the spike-train, using 60°-bins with window-length of 4 cycles. This type of autocorrelation analysis is termed here 'phase autocorrelation'. If a neuron is exhibiting phase-precession, its phase autocorrelation will have peaks at a higher rate than the LFP cycles (i.e., the autocorrelation peaks [red arrowheads in Figure 4D-middle] will occur before the LFP cycles [green dashed vertical lines in Figure 4D-middle]). For CA1 data, we used here the same 25% threshold for LFP power as for the previous analyses; for MEC data, where the LFP had lower amplitude, we used a higher threshold for LFP power (75% power), because this phase-precession analysis is sensitive to phase-estimation errors (since in order to assess phase-precession, several consecutive cycles need to have reliable phase estimates). For the same reason, in the phase-precession analyses we used a narrower band to filter the LFP signal of the bat data (1–6 Hz) – in order to further remove small rapid fluctuations that may corrupt the phase-estimation. To test for the significance of phase-precession, we computed the power spectrum of the phase-autocorrelation within a 4-cycles window, and then shuffled the spike phases 1,000 times, as follows. Within each LFP cycle separately (on a cycle-by-cycle basis), we rigidly shifted the phases of all the spikes occurring within that cycle by a random value (uniform random circular shift between 0–360°), and then calculated the power-spectrum for each shuffle. This cycle-by-cycle shuffling procedure disrupted any possible relation between spikes and LFP-phase, while maintaining most of the neuron's slow temporal dynamics (behavior-related) and rapid spike dynamics (bursts). The cell was regarded as significantly phase-precessing if the highest significant spectral peak in the power-spectrum of the phase-autocorrelation (i.e., the highest of the spectral peaks that exceeded the 95% confidence interval of the shuffles) occurred at a frequency > 1 (namely spike-fluctuation rate was higher than LFP-fluctuation rate). We only included in this analysis those neurons whose maximal value of the autocorrelation was ≥ 5 spikes.

To test for *phase-coding* of position (Figure 4G, two left panels), we used bat LFP recordings taken in 2D crawling arenas (where we had good LFP data), and transformed the 2D behavior of the bat into 1D behavior, as follows. For each place-cell we considered the position of the spatial bin with the highest firing-rate as the place-field center. Then, for each individual 2D trajectory that passed within a 25-cm radius from the place-field center, we defined the 1D position of the animal as the Euclidean distance from the animal to the point on the bat's trajectory that was closest to the field center (the 'trajectory center-point') – assigning negative and positive signs to positions before and after passing the trajectory center-point, respectively. This 1D position was plotted on the x axis of the phase-by-position plot (Figure 4G, left). We then used a standard method to quantify phase-precession (Foster and Wilson, 2007; Hafting et al., 2008; Brun et al., 2008; Mizuseki et al., 2009): We found the regression line that maximizes the explained variance (R^2) of the phase-by-position plot, for different rigid circular shifts of the spike-phases. To test for significance of this correlation, we shuffled 1,000 times the spikes by randomly permuting their identity, and calculated for each shuffle the regression line as before. A cell was defined as significantly phase-coding if the explained variance (R^2) of the phase-by-position plot in the real data was larger than in 95% of the shuffles.

The binned 'firing-rate map' for phase-by-position (Figure 4G, middle) was computed by binning the data into phase × position bins (with bin-size of 20° phase × 1.5 cm); we counted the number of spikes emitted by the cell in each bin, as well as the total time spent by the bat in that bin. These two maps (spike-count and time-spent) were then individually smoothed using a Gaussian kernel with standard deviation of $\sigma = 1.5$ bins (taking care of the circularity of the phase variable). The firing-rate map was computed by dividing bin-by-bin the two smoothed maps of spike-count and time-spent.

Lastly, we applied a second type of analysis to detect phase-coding – an analysis that does not necessarily require a linear correlation between phase and position, but rather checks for significant phase-shift between two distinct spatial positions. For each cell, we divided its spikes into two equal sets, based on the median 1D spatial position of the spikes – and then calculated the

spike-triggered average LFP for each spike-set: i.e., we compared LFP for early positions versus late positions (red versus green curves, respectively, in Figure 4G-right; see population summary in Figure 4H; the LFP was filtered here either between 1–6 Hz (Figure 4H, main plots) or between 1–10 Hz (Figure 4H, insets)). To test for significant LFP phase-shift between the two spatial positions, we computed the root-mean-square (r.m.s.) of the differences between the two spike-triggered averages (red and green) within a $\pm$ 200 ms window – and compared it to the r.m.s. calculated for 1,000 shuffles (spike-identity permutation); a neuron was defined as exhibiting significant phase-coding of the animal's position if the r.m.s. for the real data was larger than the r.m.s. in 95% of the shuffles. We also conducted population analysis (Figure 4H), whereby we computed the Pearson correlation of LFP traces that occurred around pairs of spikes emitted at either different positions (early versus late positions), or for pairs of spikes emitted at similar positions (early versus early positions or late versus late positions). Pooling these correlations across all significant cells showed that the correlations are positive for similar positions (Figure 4H, cyan) and negative for different position (Figure 4H, magenta).

QUANTIFICATION AND STATISTICAL ANALYSIS

Statistical tests were parametric, except where indicated; t tests were two-sided. We did not perform tests for Gaussianity of the data. Bootstrap shuffling of spikes-trains was used to assess the presence or absence of oscillations. Statistical testing was performed in MATLAB (Mathworks).

We analyzed here the following datasets that we collected from bats: (i) CA1 interneurons recorded from bats flying back-and-forth in a 1.5-m linear flight setup (n = 38 cells from 3 bats), or from a bat crawling on an elevated 40 × 40 cm platform (n = 6 cells from 1 bat). (ii) Hippocampal CA1 place cells recorded during 2D-crawling in either a 117 × 117 cm square arena or a 62 × 62 cm square arena (n = 42 cells from 3 bats). (iii) Hippocampal CA1 place cells recorded during 3D-flight in a large 5.8 × 4.6 × 2.7 m flight-room (n = 55 cells from 5 bats). (iv) MEC grid cells recorded during 2D-crawling in a 117 × 117 cm square arena (n = 25 cells from 3 bats). In addition, we analyzed two publicly available neuronal datasets from rats (see details above).

DATA AND SOFTWARE AVAILABILITY

All computer code and all data are archived on the Weizmann Institute of Science servers, and will be made available upon a reasonable request to the Lead Contact (nachum.ulanovsky@weizmann.ac.il).
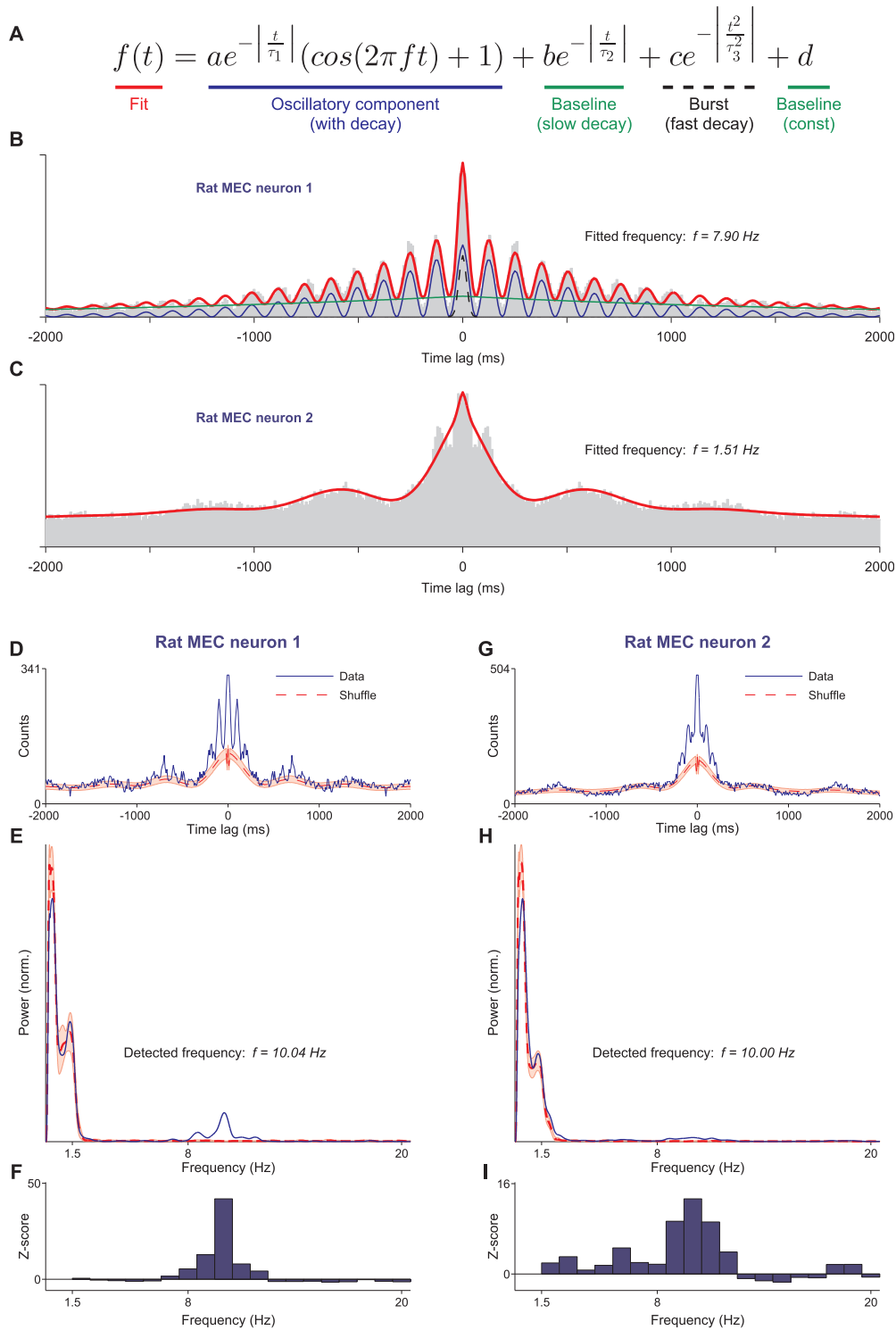
A

$$f(t) = ae^{-\left|\frac{t}{\tau_1}\right|}(cos(2\pi ft) + 1) + be^{-\left|\frac{t}{\tau_2}\right|} + ce^{-\left|\frac{t^2}{\tau_3^2}\right|} + d$$

<u>Fit</u> <u>Oscillatory component (with decay)</u> <u>Baseline (slow decay)</u> <u>- - - - - Burst (fast decay)</u> <u>Baseline (const)</u>

B

Rat MEC neuron 1

Fitted frequency: f = 7.90 Hz

Time lag (ms)

C

Rat MEC neuron 2

Fitted frequency: f = 1.51 Hz

Time lag (ms)

D Rat MEC neuron 1

Counts — Data, - - - Shuffle

Time lag (ms)

G Rat MEC neuron 2

Counts — Data, - - - Shuffle

Time lag (ms)

E

Power (norm.)

Detected frequency: f = 10.04 Hz

Frequency (Hz)

H

Power (norm.)

Detected frequency: f = 10.00 Hz

Frequency (Hz)

F

Z-score

Frequency (Hz)

I

Z-score

Frequency (Hz)

Figure S1. Temporal Fit and Spectral Analyses Methods, Related to Figure 2

(A–C) Temporal fit analysis.

(A) Fit equation: each component of the fit is marked by a different color, corresponding to the colors of the line-plots in B, which graphically depict these components.

(B) Autocorrelation of a rat MEC neuron (gray bars), with an overlaid decaying-sinewave fit (red line). The fit was decomposed here to its components from A, denoted by the different colors.

(legend continued on next page)

(C) Autocorrelation of a rat MEC neuron that exhibited a low-frequency oscillation, demonstrating that the fit can also detect low frequencies, if they exist.

(D–I) spectral analysis.

(D and G) Autocorrelations of two example neurons from rat MEC (blue), together with the spike-train autocorrelations of shuffled data (dashed red line – mean, red area – SD). These are different neurons than those shown in B and C. The shuffled autocorrelation eliminated the rapid theta oscillations, but it otherwise retained the general shape of the autocorrelations – including the slow modulation exhibited by these neurons, which is likely due to the repetitive passage of the animal through the neuron's grid-fields. (Note that the period of this modulation, which is 700 ms for the neuron in Figure S1D, is almost exactly equal to the ratio of the grid spacing [90 cm for this cell] divided by the rat's median running-speed in the central part of the linear track [137 cm/s for this day]; the distribution of the running-speeds had a coefficient of dispersion of 0.29, indicating a relatively constant running speed – and therefore the repetitive passages of the animal through the grid-fields could create the observed temporally repetitive firing).

(E and H) Power spectrum of the autocorrelations from D and G, showing the strong theta-rhythmicity of these two rat neurons, indicated by the peak at ~10 Hz (blue) being significantly higher than the shuffled data (dashed red line – mean, red area – SD) – suggesting the existence of genuine neural oscillations at ~10 Hz.

(F and I) Plot of the z-scores for each frequency-bin of the power spectrum; the highest value in this plot indicates the most significant frequency-bin. For these two neurons from rat MEC, it identified the most prominent oscillation at ~10 Hz for the left neuron (with z-score = 42) and at 10 Hz for the right neuron (with z-score = 13). By contrast, note that the low-frequency spectral peak in E was not significant; this suggests that this low-frequency peak resulted most likely from the repetitive passage of the animal through the neuron's grid-fields – and does not represent a real neural oscillation.

A

Short cycles
Long cycles

B

CA1

MEC

Cycle duration (s)

C

Example

Without thresholding
Oscillation index=0.019

Same example neuron
with thresholding
Oscillation index=0.007

D
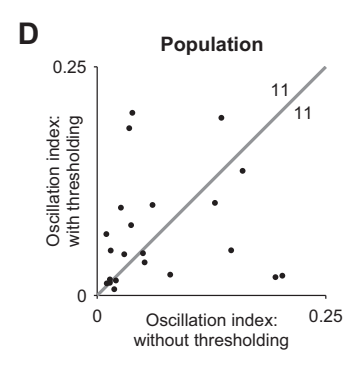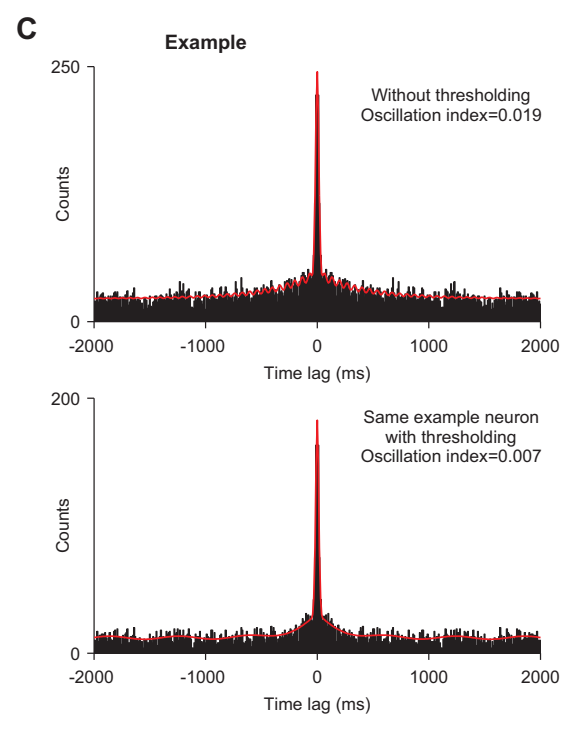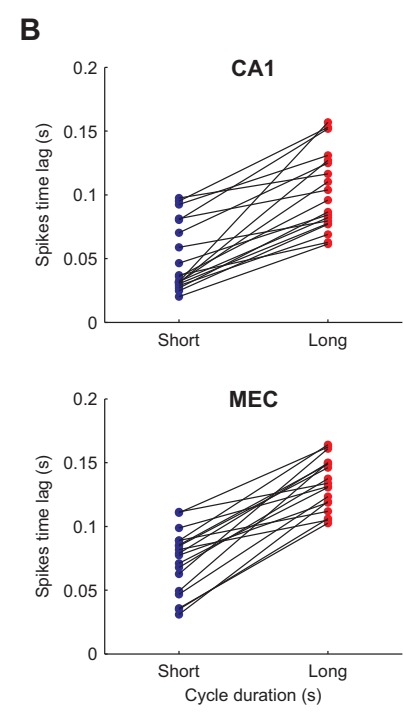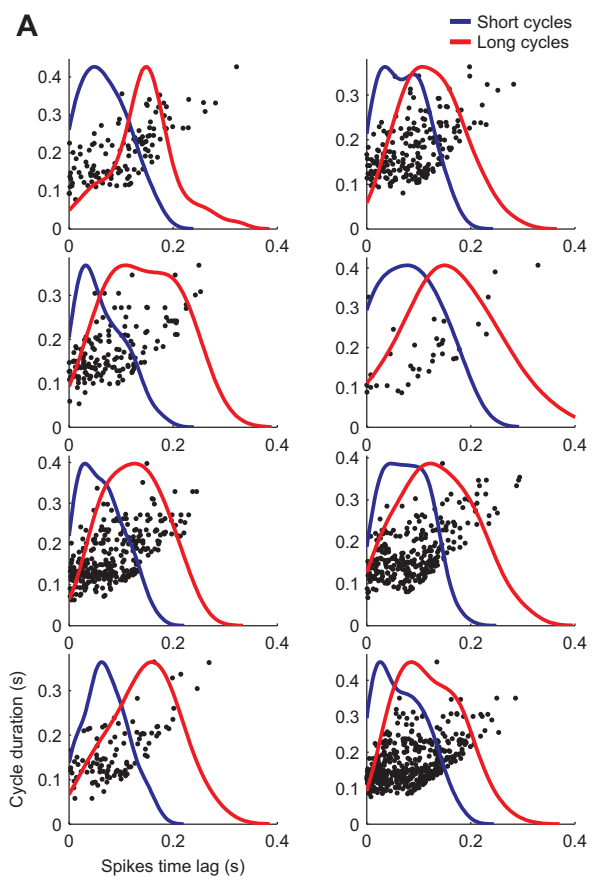
Population

(legend on next page)

Figure S2. Analysis of Phase Locking in Short Cycles versus Long Cycles, and Comparison of Autocorrelations When Using All Spikes versus When Using Spikes Emitted during High-Amplitude LFP, Related to Figures 2 and 3

(A and B) Analysis showing that the spikes during long cycles occur later than spikes during short cycles – suggesting that the spike-locking in short cycles is *not* a truncated version of the spike-locking in long cycles; this indicates that bat neurons exhibit phase-locking, rather than time-locking.

(A) Eight examples of cells from bat CA1 and MEC, plotting the cycle duration versus spike-time-lag within the cycle (dots = spikes). Clear correlations are seen in the scatters in all the eight examples: Note especially the lack of early spikes in long cycles (almost no dots in the upper-left corners of the scatters), demonstrating that the spikes during long cycles occur later than spikes during short cycles. Superimposed blue and red curves: kernel density function distributions of spike lags for cycles shorter than 0.2 s (blue) and for cycles longer than 0.2 s (red). The kernel density functions were normalized to their peak. Example cells #3, 5, 8 are from CA1, and example cells #1, 2, 4, 6, 7 are from MEC.

(B) Population analysis showing the peak time lag in long cycles (red dots) versus short cycles (blue dots) in bat CA1 (top) and bat MEC (bottom). Plotted for all the significantly phase-locked neurons. In all cases, the peak density of spikes occurred later in long cycles than in short cycles.

(C and D) We tested here an alternative hypothesis – namely, that the observed phase-locking in bat CA1 neurons (Figures 3D and 3F) might result from a transient true rhythmic process (oscillatory bouts) that was revealed by the LFP power-thresholding which we applied in the phase-locking analysis (whereby we took only LFP cycles with a power > 25th percentile of the LFP power in the entire recording: see the STAR Methods). To test this alternative hypothesis, we used here a fit-analysis for the autocorrelations, similar to Figure 2: we used for this either all the spikes, as in Figure 2 (without power-thresholding) – or used only the spikes that were based on a power-thresholded LFP (which were included in the phase-locking analysis in Figures 3D–3G).

(C) Example cell from bat CA1, showing spike-train autocorrelations (black) with fitted decaying sinewave (red), computed for all spikes (top) and after applying power-thresholding for the same neuron (bottom). Both autocorrelations exhibited a similar low value of the oscillation index: there was no increase in oscillation-index in the bottom panel as compared to the top panel. This lack of change argues against this alternative hypothesis.

(D) Population comparison (dots = neurons). Plotted is the oscillation index when using power-thresholding (y axis) versus the oscillation index without any power-thresholding (x axis); plotted for all the bat CA1 place-cells that passed the inclusion criteria for the fit analysis in both conditions (n = 22 cells; see the STAR Methods). Note the exact same number of neurons above versus below the diagonal (numbers indicated on the graph) – suggesting that the oscillation index does not systematically increase or decrease after applying power-thresholding (paired t test: p = 0.94; sign test: p = 1). This argues against the hypothesis that power-thresholding reveals transient rhythmicity in the bat data.
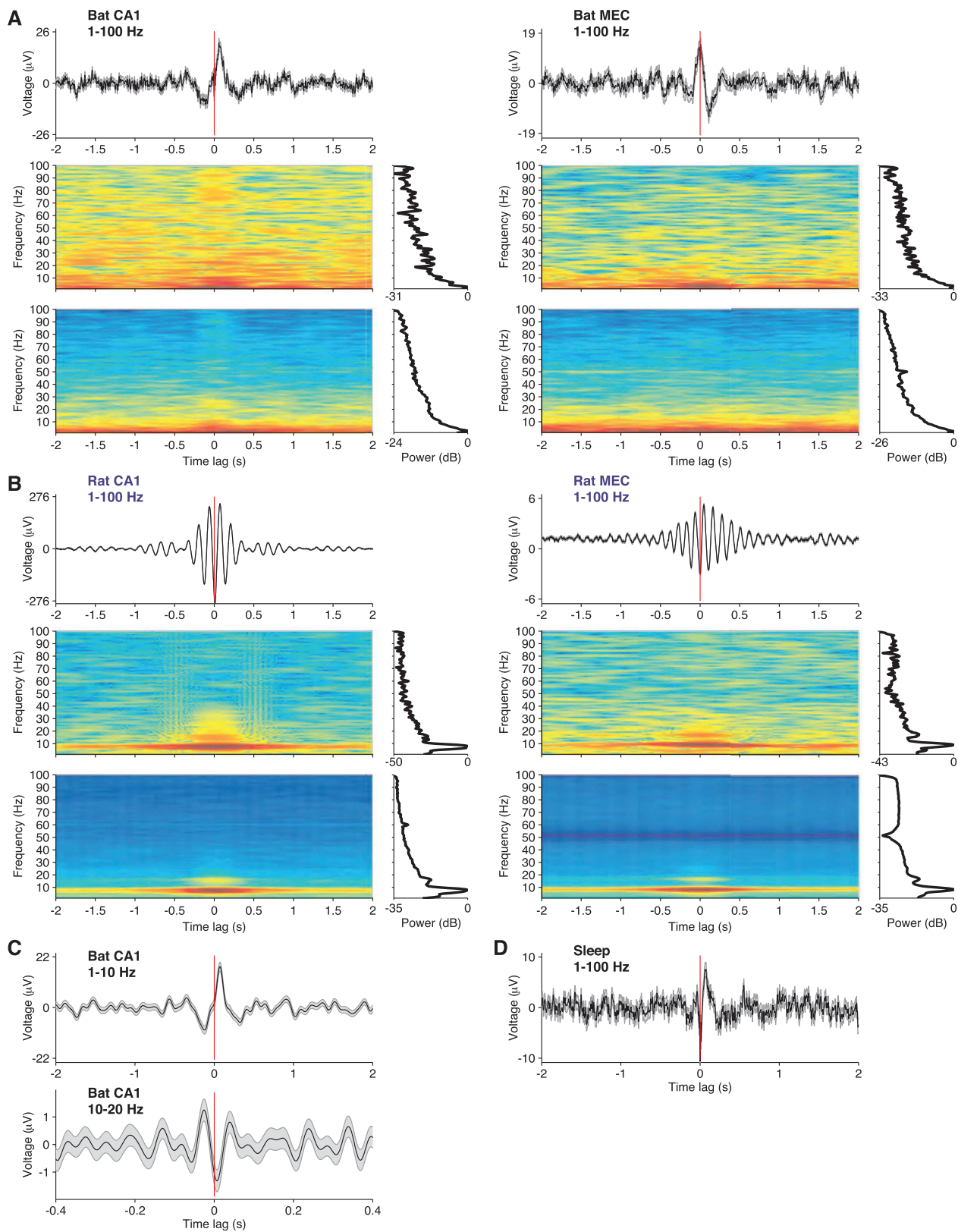
Figure S3. Population Average Spike-Triggered LFP and Its Spectrogram, Related to Figure 3

(A) Top: Spike-triggered LFP average for the bat CA1 neurons that exhibited significant phase-locking (n = 19, left), and for the bat MEC neurons that exhibited significant phase-locking (n = 18, right); gray area, mean ± SEM; the LFP was filtered between 1–100 Hz prior to averaging. The time of the spikes is indicated by the red line (time lag: t = 0). Middle: spectrogram of the spike-triggered LFP average plotted above, computed using a 1 s Hamming window. Bottom: averaged spectrogram across neurons, where we first computed the spectrogram for each neuron separately – and then computed the average of all these spectrograms (this was done to avoid possible phase-cancellations between neurons with different preferred-phases). The marginal of each spectrogram is plotted to the right of the spectrogram.

(B) Top: Spike-triggered LFP average for the rat CA1 neurons that exhibited significant phase-locking (n = 61, left), and for the rat MEC neurons that exhibited significant phase-locking (n = 251, right); the LFP was filtered between 1–100 Hz – as in the bat; same graphical conventions as in A. Middle: Spectrograms of the spike-triggered LFP average, computed as in A. Bottom: averaged spectrograms across neurons, computed as in A. Note the clear theta-oscillations in the rat spike-triggered LFP (B, top) before and after each spike, with oscillations lasting many theta-cycles – in stark contrast to the lack of such oscillations in bats (A, top). The oscillations in the rat were apparent also in the spectrograms of spike-triggered LFP (B, bottom); no such oscillations were apparent in the bat spectrograms (A, bottom). Rat CA1 data courtesy of G. Buzsáki. Rat MEC data courtesy of M.-B. Moser and E.I. Moser. We examined here all the rat CA1 and rat MEC neurons that had LFP recordings, and included in the analysis all the neurons that exhibited significant phase-locking.

(C) Spike-triggered LFP average for the bat CA1 neurons that exhibited significant phase-locking (n = 19), plotted as in (A) – with the only difference from (A) being that here the LFP was filtered between 1–10 Hz prior to averaging (top) or filtered between 10–20 Hz prior to averaging (bottom). Note the different time-scales at the top versus the bottom.

(D) Spike-triggered LFP average during sleep sessions, computed for the bat CA1 neurons that exhibited significant phase-locking (n = 19) – same neurons as in panels A and C. The LFP was filtered between 1–100 Hz prior to averaging. We excluded from this analysis sharpwave-ripple epochs (±10 s epochs were removed) around each sharpwave-ripple), in order to exclude any possible ripple-related locking. Gray area, mean ± SEM.
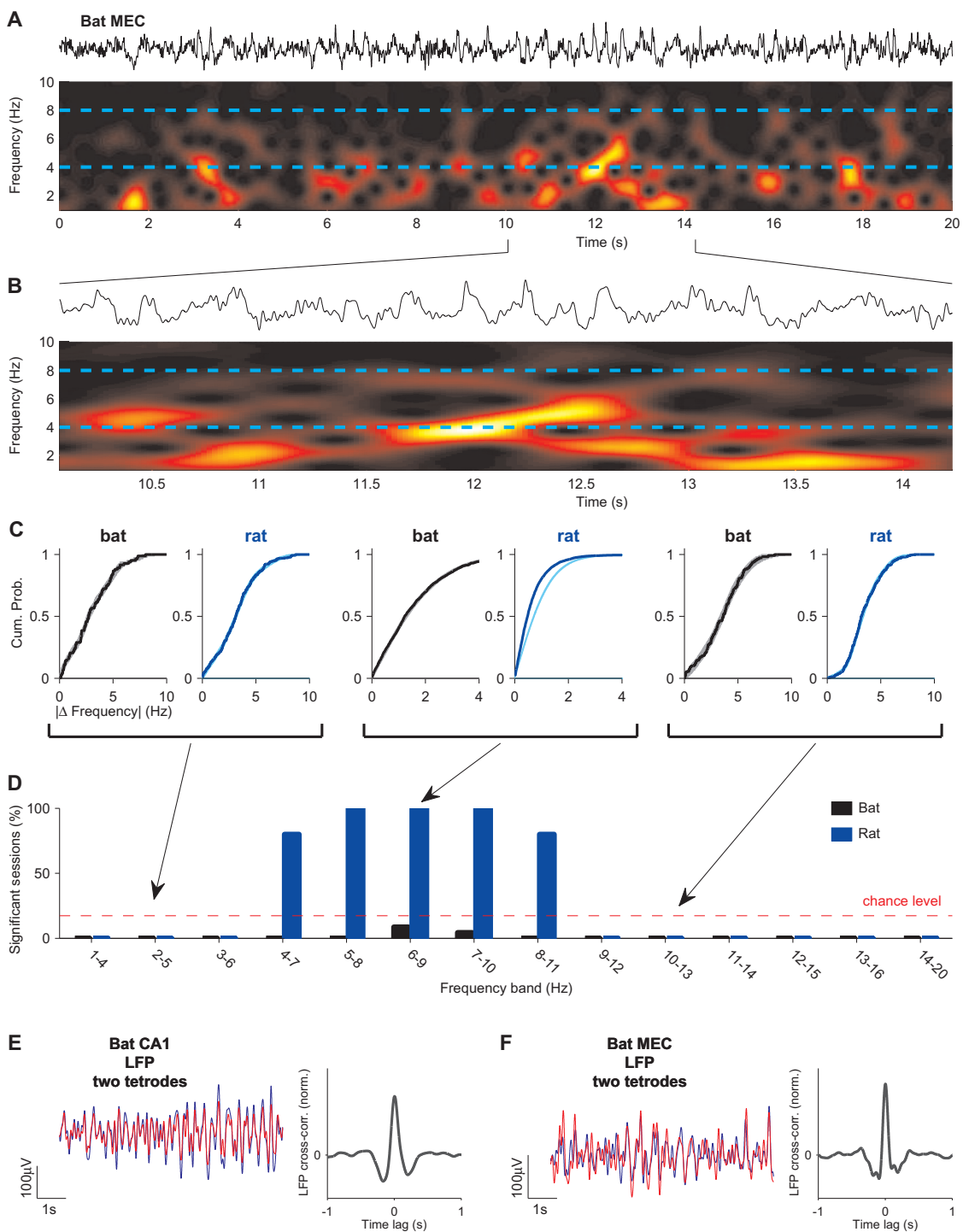
Figure S4. Spectrogram of LFP Recorded from Bat MEC, Analysis of LFP Fluctuations in Different Frequency Bands, and LFP Recorded Simultaneously on Pairs of Tetrodes, Related to Figure 3

(A and B) spectrogram of LFP recorded from bat MEC.

(A) Top, LFP trace from MEC of a crawling bat. Bottom, spectrogram (frequency versus time) of the LFP trace.

(B) Zoom-in on the data in A, showing a theta-bout at t ∼12 s: a momentary passage of the LFP signal through the theta band (4–8 Hz; dashed horizontal blue lines).

(legend continued on next page)

(C and D) Analysis of LFP fluctuations: Same analysis as in Figure 3J, but performed separately for specific frequency bands (3-Hz wide bands). Data were included only for cycles that occurred during putative bouts. The separation into bands was done by the frequency of the first cycle in each pair of cycles: e.g., the 4–7 Hz band signifies that the first cycle was in the 4–7 Hz range – but the subsequent cycle in the bout could be at *any* frequency.

(C) Examples of cumulative distributions of the changes in the frequencies of consecutive LFP cycles, computed only for cycles that occurred during putative bouts; in the left pair of plots we included only pairs of cycles in which the first cycle was in the 2–5 Hz frequency band (see arrow to [D]) – while the subsequent cycle could be at *any* frequency; middle pair of plots, likewise for the 6–9 Hz frequency band; right pair of plots, 10–13 Hz frequency band. Dark-blue line, rat data; black line, bat data; light-blue area and gray area, 95% confidence intervals of the shuffled data for rat and bat, respectively.

(D) Population analysis, showing the percentage of significant sessions, in which the cycle-to-cycle frequency differences in the real data were smaller then in shuffled cycles. Rat data showed highly significant results in the theta frequency range, but not outside of this range (blue bars) – signifying that in the theta frequency range, the cycle-to-cycle frequency variability in rat CA1 is lower than expected by chance. By contrast, in the bat CA1 data, in each of the analyzed frequency bands, from 1 Hz to 20 Hz, the LFP frequencies varied from cycle-to-cycle as much as a random shuffle (black bars) (the black bar in the 6–9 Hz frequency range represents 2/23 recording sessions that were significant at the 5% significance level – but we note that this bar is in fact not significant, because it can easily be obtained by chance: the probability of obtaining 2/23 significant sessions at the 5% per-session significance level is: $p = 0.32$, Binomial test). Dashed line, chance level for bat data (binomial test).

(E and F) LFP fluctuations are correlated between different tetrodes.

(E) Example from CA1. Left, LFP traces from bat CA1, filtered between 1–10 Hz, from two tetrodes (red and blue) – during a session in which place-cells were recorded simultaneously on both tetrodes. Note the LFPs on the two tetrodes were highly correlated. Tetrodes' spatial separation: 250 μm. Scale bars: 1 s, 100 μV. Right, cross-correlation of the LFP signals from these two tetrodes, computed over the entire recording session. The peak at time-lag 0 indicates that the LFPs recorded on both tetrodes were correlated. The cross-correlation is biphasic, and not oscillatory – as expected from non-rhythmic signals.

(F) Example from MEC. Left, LFP traces from two tetrodes in bat MEC, showing high correlation between the LFPs. During this session grid-cells were recorded simultaneously on both tetrodes. Tetrodes' spatial separation: 550 μm. Scale bars: same as in (E). Right, cross-correlations of the LFP signals from these two tetrodes, computed over the entire session.

A — Example of phase precession, Example of phase locking

B

C

D

E
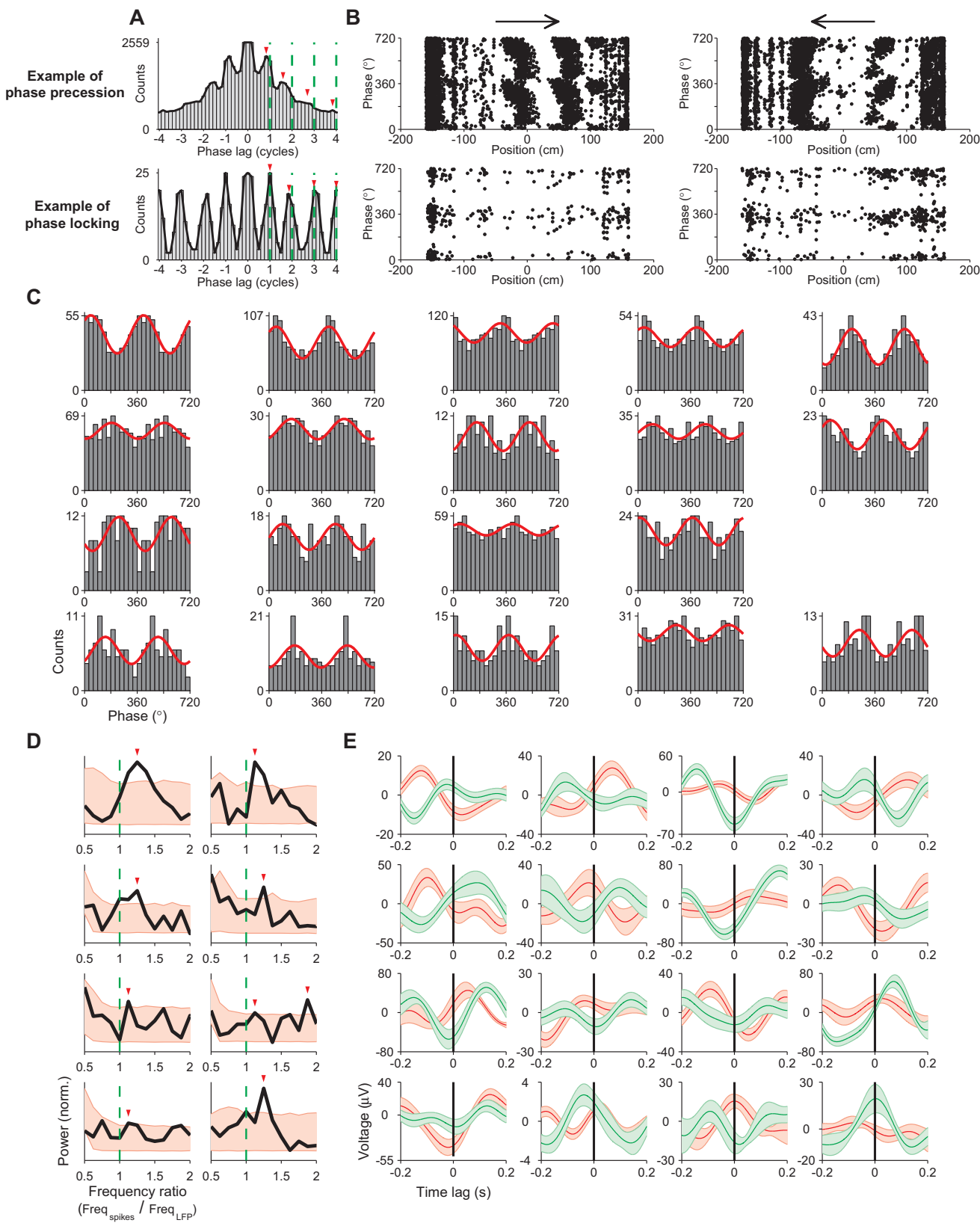
(legend on next page)

Figure S5. Phase Autocorrelation Analysis of Rat MEC Cells and Plots of All the Significantly Phase Locking and Phase Coding Cells in the Bat, Related to Figures 3 and 4

(A and B) Rat data. Shown are examples of two rat neurons (rows): a phase-precessing neuron (top) and a phase-locked neuron (bottom), recorded during 1D linear-track locomotion in rat MEC. Data courtesy of M.-B. Moser and E.I. Moser.

(A) Phase autocorrelation analysis. Top example – a phase-precessing cell: note the peaks of the autocorrelation (red arrowheads) are occurring faster than the LFP cycles (green dashed vertical lines), indicating phase-precession. Bottom example – a phase-locked cell: the peaks of the autocorrelation are occurring precisely at integer multiples of the LFP cycle (green dashed vertical lines) – indicating phase-locking without phase-precession.

(B) Phase-versus-position plots for the two example neurons from (A). Two cycles are shown on the y axis, for clarity. Top neuron: spike phase is negatively correlated with the rat's location on the 1D linear track, along the running direction (arrows) – indicating phase-precession. Bottom neuron: spikes are strongly locked to the LFP phase, but are independent of position – indicating phase-locking without phase-precession. These two examples illustrate our 'phase-autocorrelation' analysis approach: in the top neuron, where the position-phase plot (B) shows phase-precession, this phase-precession is captured also in our phase-autocorrelation analysis (A). Conversely, in the bottom neuron, which shows no phase-precession in (B), also no phase-precession is captured in our analysis in A.

(C–E) All the bat neurons that exhibited significant phase-locking (C), significant phase-precession (D) and significant phase-coding (E).

(C) Phase-locking histograms for all the bat neurons that exhibited significant phase-locking (n = 14 place cells in CA1 [first three rows] and n = 5 grid cells in MEC [fourth row]). Plotted as in Figures 3D and 3F.

(D) Spectra of the phase-autocorrelations for all the seven CA1 neurons that showed significant phase-precession (7 first panels) and 1 MEC neuron that showed significant phase-precession (bottom-right panel). Black line, spectrum of the phase-autocorrelation of the real spike-train; red area, 95% confidence intervals for the spectra of the shuffled spikes. Red arrowheads denote the highest significant spectral peaks for which the frequency-ratio (Freq $_{spikes}$ / Freq $_{LFP}$) was larger than 1 – indicating phase-precession. The top-right and bottom-right panels correspond to the two example neurons shown in Figures 4D and 4E, respectively.

(E) Plots of spike-triggered LFP averages, calculated separately for spikes occurring in early positions (red) versus late positions (green) – for all the bat neurons that exhibited significant phase-coding in CA1 (n = 16 place cells). Plotted as in Figure 4G, right. Red and green areas, mean ± SEM.